理學博士 學位論文

Fabrication of carbon nanomaterials using thermal plasma jet and their applications

열 플라즈마 장치를 이용한 탄소나노소재 제조 및 응용

2017 年 8 月

서울대학교 대학원

화학부 물리화학 전공

이 명 우

Fabrication of carbon nanomaterials using thermal plasma jet and their applications

열 플라즈마 장치를 이용한 탄소나노소재 제조 및 응용

지도교수 : 서 정 쌍

이 論文을 理學博士 學位論文으로 提出함

2017 년 8 월

서울大學校 大學院

化學部 物理化學 專攻

이 명 우

이명우의 理學博士 學位論文을 認准함

2017 년 8 월

위 원 장 홍 병 희 (인)

부위원장 서 정 쌍 (인)

위 원 이 성 훈 (인)

위 원 김 지 환 (인)

위 원 강 위 경 (인)

Abstract

Fabrication of carbon nanomaterials using thermal plasma jet and their applications

Myung Woo Lee
Department of Chemistry
(Major : Physical Chemistry)
The Graduate School
Seoul National University

Recently, carbon nanomaterials are widely studied and used in various applications including electronic devices, solar cells, and nanobiomedicine. Carbon nanomaterials have been mainly determined by their shapes: zero-dimensional fullene, one-dimensional carbon nanotube, and two-dimensional graphene. In addition to listed materials, there are various carbon nanomaterials such as graphene quantum dots (GQDs), onion-type carbon, nanodiamond, amorphous carbon, and carbon dots. Each of carbon nanomaterials has different physical and chemical properties by their structure. Characteristics of carbon materials have been utilized in the need of application. However, the commercialization of carbon nanomaterials stayed for a long time due to diffculty in the technology of mass production. We have developed mass production of carbon nanomaterials using

thermal plasma jet and utilized the product for application.

Graphene has generated tremendous interest over the past decade because of its extraordinary properties and potential applications. In this work, dispersible graphene flakes were successfully fabricated *via* a one-step process using a thermal plasma jet system. The graphene flakes fabricated by injection of ethylene gas as a carbon source (500 sccm) were very pure, contained no oxygen, and were few layered. Although their average size was larger than 100 nm, they were well-dispersed in organic solvents by sonication. The production rate based on the collected amount was approximately 1.5 g/h. As a representative application, thin films of the graphene flakes were fabricated on fluorine-doped tin oxide (FTO) glass using three deposition techniques. The resulting dye-sensitized solar cell with a graphene flake/FTO counter electrode exhibited a power conversion efficiency of 9.03%, which was similar to the efficiency of the solar cell with a conventional Pt/FTO counter electrode. Therefore, our graphene flake/FTO electrode could be used as a substitute for the conventional Pt/FTO counter electrode for DSSCs as graphene flakes are much less expensive than Pt. In addition to this specific application, dispersible graphene could be used in the fabrication of composites as well as various energy storage, sensor, and electronic devices.

Graphene is a zero band gap semiconductor, which reduces its electronic and optoelectronic properties almost impossible to use for

device applications. However, the GQDs, which are graphene sheets smaller than 100 nm, possess strong quantum confinement and edge effects. The former effect allows the bandgap of GQDs to be controlled by modifying their size, and the latter effect causes the GQDs to be dispersed in common solvents. We reported a size-controllable method for GQDs by a gas phase collision reaction of carbon atoms using thermal plasma jet. A carbon tube was generated by injecting a large amount (2,500 sccm) of ethylene gas continuously into Ar plasma. A carbon tube was attached to an anode and ethylene gas was flowed continuously as a carbon source into a torch through a gas flow meter. The production rate of GQDs was about 4 g/h, and the average size of GQDs was controlled by varying the length of the carbon tube attached. However, there is no quantum confinement effects to control the band gap of GQDs by modulating their size. Thus, we focused on strong edge effects of GQDs.

When a graphene sheet is cut along zigzag lines, carbene edges having two unshared valence electrons at each edge carbon atom are made, while along armchair lines carbyne edges having carbon triple bonds are made. Carbene and carbyne edges have polar and nonpolar characters, respectively. 90 degree corners are made when armchair and zigzag lines are encountered, while 120 degree corners are made when the same type lines are encountered. Therefore, hexagonal GQDs are made when the same type cutting lines are encountered, at all corners, while rectangular GQDs are made when different type cutting lines are encountered. We have separated three kinds of

GQDs: Zigzag GQDs having only carbene edges were dispersed in polar solvents and had basically hexagonal shapes. Armchair GQDs having only carbyne edges were dispersed in nonpolar solvents and had also basically hexagonal shapes. Hybrid GQDs having both carbyne and carbene edges in each dot were dispersed in both polar and nonpolar solvents and had rectangular shapes. The photoluminescence and photoluminescence excitation spectra of hybrid GQDs responded to the combination of the spectra of zigzag and armchair GQDs. The absolute quantum yields of three kinds of GQDs are relatively very high. For a 2.5 L/min injection rate of ethylene gas, the production rate of GQDs is about 4 g/hour. The relative abundance of armchair, zigzag and hybrid GQDs is 96.9, 2.7, and 0.4%, respectively. The producted GQDs were used in nanobiomedicine such as bioimaging and photodynamic therapy.

Onion-type carbon and nanodiamond, before discovery of graphene and carbon nanotube, were one of the most promising carbon nanomaterials in the past. However, research of onion-type carbon stayed for a long time due to high-cost fabrication methods. We have fabricated onion-type carbon by a gas phase collision reaction of carbon atoms using thermal plasma jet. A carbon atomic beam was generated by injecting a large amount of ethylene gas continuously into Ar plasma. A carbon tube was attached to an anode and ethylene gas was flowed continuously as a carbon source into a torch through a gas flow meter. The production rate of onion-type carbon was about 36 g/h and the average size was 15 - 20

nanometers, showing a lattice like the structure of the onion. The produced onion-type carbon was well dispersed in organic solvent and absorbed all light from ultraviolet to near-infrared region. The onion-type carbon was used for photothermal therapy, which destroys cancer cells by generating heat with light irradiation using nanoparticles, due to its low-toxicity and the heat generated by light irradiation. In the absence of light, the dispersed solution at concentration up to 0.5 mg/ml did not show obvious toxicity to cells. *In vitro* photothermal effect of onion-type carbon led to cells destruction after 10 min of laser irradiation at 2 W/cm^2.

Key words: Carbon nanomaterials, Thermal plasma jet, Graphene, Graphene quantum dots, Onion-type carbon, Photodynamic therapy, Photothermal therapy, Dye-sensitized solar cell

Student Number: 2014-22408

Contents

List of Tables

List of Figures

Chapter 1

Introduction

1. 1. Carbon materials

New demands for high-speed electronics, renewable energy, and biomedicines have contributed great attention to researchers. Thus, they have discovered and developed new types of nanomaterials. Carbon materials are well-known as various structures by allotropes of carbon from sp^3 to sp^2 hybridized carbon. It is also possible to form mixed state such as amorphous carbon and nanocrystalline diamond. Carbon based nanomaterials of new materials have been paid special attention due to their inherent structure and physical properties. However, the commercialization of carbon nanomaterials stayed for a long time in the insufficient technology of mass production. We have developed mass production of carbon nanomaterials by using thermal plasma jet and used carbon nanomaterials for solar cells and bio-medical applications.

1. 2. Graphene Quantum Dots (GQDs)

1. 2. 1. The properties of GQDs and synthetic methods

Graphene quantum dots (GQDs), which are graphene sheets smaller than 100 nm, possess strong edge effects and quantum confinement.[1] The former effects allow dispersion in solvents like ethanol, while graphene is not dispersible in common solvents. Graphene is a zero band gap semiconductor, which reduces its electronic and optoelectronic properties almost impossible to use for device applications.[2] However, the quantum confinement allows the bandgap of GQDs to be controlled by modulating their size.[3-5] Due to the band gap, GQDs could exhibit photoluminescence.[6-8] Dispersible property and controlled nonzero bandgap of GQDs make them excellent materials for the construction of nanoscale optical[9-11], bioimaging[12-14], and electronic devices[15]. Controlled fabrication methods for stable graphene nanostructure provide a chance to investigate outstanding optical[16-22] and transport[23] properties of these structures. Both top-down and bottom-up methods have been used to prepare GQDs. Cut of graphene sheets[1] or graphene oxide sheets[24-27] or carbon fibers[10] or self-assembled block

copolymer[28] or tattered graphite[29] or carbon black[30] or coal[31] corresponds to a top-down method, while self-assembling of aromatic carbons followed pyrolysis,[32] cyclodehydrogenation of polyphenylene precursors[33,34], microwave assisted hydrothermal method[35], tuning the carbonization degree of citric acid[36], and pulsed laser synthesis method from benzene[37], correspond to a bottom-up method. Cage-opening of fullerenes[38], may be categorized as a third method. However, these methods have some drawbacks in the aspects of low-cost production, size-controllable fabrication, and mass production.

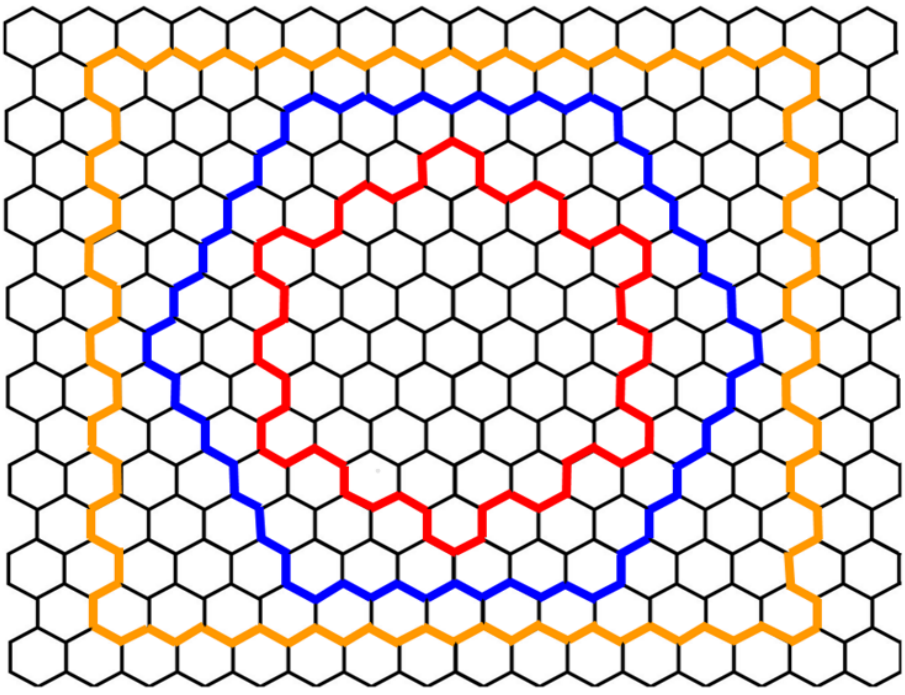

Figure 1. 1. Model of three kinds of graphene quantum dots; red, blue and yellow are armchair, zigzag, and hybrid GQDs, respectively.

1. 2. 2. Three kinds of GQDs

On a graphene sheet,[39] a 120 degree corner is made when two armchair lines or two zigzag lines are encountered, while a 90 degree corner is made when armchair and zigzag lines are encountered (see Figure 1.1). Therefore, in tailoring a graphene sheet, hexagonal GQDs are made when the same type cutting lines are encountered at all corners, while rectangular GQDs are made when different type cutting lines are encountered at all corners. When a graphene sheet is cut along an armchair line, carbon triple bonds are made at edges (see Figure 1.2). It is called carbyne, which may have a nonpolar characteristic due to carbon triple bonds at edges.[40] Along a zigzag line, two unshared valence electrons are made at each edge carbon atom. It is called carbene, which may have a polar characteristic due to lone pair electrons. Therefore, three kinds of GQDs could be distinguished by their shape and edge structure or dissolving property; two kinds of hexagonal GQDs dissolving either polar or nonpolar solvent, and rectangular GQDs dissolving in both polar and nonpolar solvents. For GQDs that can be dissolved in nonpolar solvent like cyclohexane and have hexagonal shapes could be named as armchair or nonpolar hexagonal (or simply nonpolar) GQDs. For GQDs that can be dissolved in polar solvent like water and have hexagonal shapes could be named as zigzag or polar

hexagonal (or simply polar) GQDs. The GQDs that can be dissolved both in polar and nonpolar solvents and have rectangular shapes could be named as hybrid or amphoteric rectangular (or simply amphoteric) GQDs. Here, we have fabricated three kinds of GQDs by a gas phase collision reaction of carbon atoms using a thermal plasma jet system[41], and proved that the basic shape and dissolving property of our three kinds of GQDs are well agreed with those predicted from the model GQDs shown in Figure 1.1. For a 2.5 L/min injection rate of ethylene gas, the production rate of GQDs was about 4 g/hour. The relative abundance of armchair, zigzag and hybrid GQDs was 96.9, 2.7, and 0.4%, respectively.

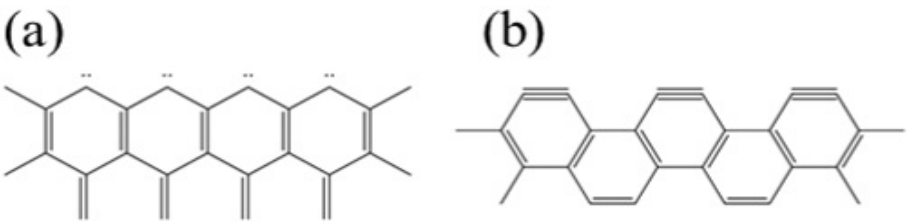

Figure 1. 2. The edge structures of (a) carbene and (b) carbyne.

1. 2. 3. Photo-induced reactive oxygen species generation upon edge type of GQD for enhanced photodynamic therapy *in vitro* and *in vivo*

Photodynamic therapy (PDT) is a treatment that involves the use of a light sensitive drug (photosensitizer; PS) and a light source to destroy the cancerous or otherwise unwanted tissue.[42,43] Photosensitizer performs the role of initiating a physical, chemical, or biological process in a non-light-absorbing substrate. It is known that reactive oxygen species (ROS) such as singlet oxygen $^1O_2$ ($^1\Delta_g$) are produced by a photosensitizer under illumination and in the presence of oxygen, cancerous cells are locally killed by ROS.[42] For clinical applications, photosensitizers need to have a high singlet oxygen ($^1O_2$) quantum yield, excellent photostability and good biocompatibility. Porphyrin, phthalocyanines and bacteriochlorin derivatives have been used as photosensitizers in PDT.[44] These organic photosensitizers possess simultaneous cancer imaging and therapy capabilities, and some of them have been approved for clinical use.[45] In terms of photostability and water dispersability, semiconductor quantum dots (QDs) are superior to organic photosensitizers.[46-48] However, the clinical application has been obstructed owing to their cytotoxicity and low ROS-generation efficiency[49-53]. Recently, Ge at al. reported that GQDs can

produce singlet oxygen *via* a multistate sensitization process, resulting in a quantum yield of ~1.3, which is used for PDT agents.[54] Their GQDs were prepared by thermal treatment polythiophene, and contained some nitrogen and sulfur in the structures. In some aspects, their GQDs were not well defined.

Recently, Lee et al. have developed a method to fabricate three types of GQDs by a gas phase collision reaction using thermal plasma jet.[55] Zigzag GQDs having only carbene edges are dispersed in polar solvents and, basically had hexagonal shapes. Armchair GQDs having only carbyne edges are dispersed in nonpolar solvents and, had also basically hexagonal shapes. The photoluminescence (PL) spectra of zigzag GQDs is observed in higher energy regions than those of armchair GQDs. The PL spectra of hybrid GQDs corresponds to the combination of the spectra of zigzag and armchair GQDs. Here, we have tested the therapy capabilities of armchair and zigzag GQDs as PDT agents.

It is known that the ground state of carbene is a triplet, while carbyne is a singlet.[40] This fact means that the ground state of zigzag GQDs is a triplet since they have carbene edges. For armchair GQDs having carbyne edges, they have a singlet ground state. The states that arise from the ground configuration of oxygen are $^3\Sigma_g^-, ^1\Sigma_g^+$ and $^1\Delta_g$. Hund' s rules tell us that $X^3\Sigma_g^-$ is the ground state. The $^1\Sigma_g^+$ singlet state is 1.63 eV [158 kJ/mol], while the $^1\Delta_g$ singlet state is 0.98 eV [94.3 kJ/mol], higher in energy than the triplet ground state of oxygen. The radiative

decay lifetime of the $^1\Delta_g$ state is 45 minutes at the very low gas pressures. However, collisions with other molecules induce much shorter lifetime, *e.g.* 14 minutes in oxygen gas at 760 torr. The decay lifetime of the $^1\Sigma_g^+$ state is 7 seconds. The $^1\Sigma_g^+$ state is rapidly converted to the $^1\Delta_g$ state in condensed media.

For armchair GQDs, the HOMO is singlet and the LUMO is triplet, while for zigzag GQDs the HOMO is triplet and the LUMO is singlet.[15] Here, we have tested the therapy capabilities of three kinds of GQDs as PDT agents. By treating cancellous cells with armchair GQDs and irradiation with 365 nm light, these cells were killed, while for zigzag GQDs, they are by exposing not killed. (see Figure 1.3)

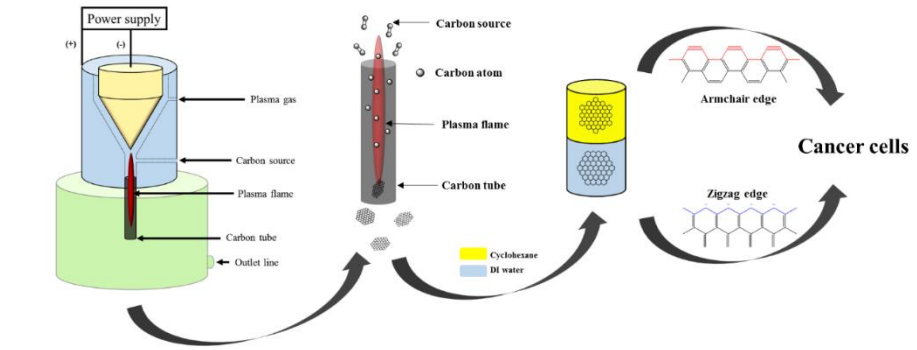

Figure 1. 3. Fabrication of GQDs by a gas collision reaction in the attached carbon tube, liquid–liquid extraction of two kinds of GQDs, and PDT *in vitro* and *in vivo*.

1. 3. Graphene flakes

1. 3. 1. The properties of graphene and synthetic method

Graphene[39], a two-dimensional material of sp^2-hybridized carbon atoms, has generated great interest over the past decade because of its extraordinary properties and potential applications.[56-59] demonstrates significant , especially in terms of electronic and optical device applications.[60-66] However, there are serious drawbacks to its application. For instance, graphene is a zero-bandgap semiconductor, which limits its electronic and optoelectronic applications,[2] and cannot be dispersed in common solvents. The properties of graphene are known to be affected by the morphology of graphene sheets, including their size, shape, and thickness.[1,67,68] GQDs, which are graphene sheets smaller than 100 nm,[1] exhibit strong quantum confinement and edge effects. The former effect allows the bandgap of GQDs to be controlled by modifying their size, and the latter effect causes the GQDs to be dispersed in common solvents. These properties make GQDs excellent materials for the construction of nanoscale optical and electronic devices.[26,69,70] However, for applications such as the fabrication of a composite, the availability of graphene that can be dispersed in solvents without significantly

degrading its conductivity through the quantum confinement effect is required. Graphene can be made dispersible in solvents by changing it to graphene oxide followed by reduction to graphene again.[59,71] However, these methods are high-cost processes, which may also degrade the properties of the graphene.

1. 3. 2. Previous articles: graphene flakes and GQDs fabricated by thermal plasma jet

We developed a method to fabricate graphene flakes[72] and GQDs[41,55] using thermal plasma jet. In both methods, a carbon tube (5-20 cm in length) is attached to the anode, and the carbon atomic beam generated by continuous injection of a carbon source into the plasma jet flows through the attached carbon tube. In the fabrication of graphene flakes, a graphite plate is placed perpendicularly approximately 10 cm away from the end of the attached carbon tube; no graphite plate is used for GQDs. The injection rate of a carbon source in the fabrication of carbon soot containing GQDs is much higher than that of graphene flakes. The growth mechanisms of flakes and GQDs also differ. When a high-density carbon atomic beam flows through the attached carbon tube, carbon soot containing GQDs is formed by gas phase collision reactions. However, when a low-density carbon atomic

beam is collided with the graphite plate, graphene is formed by epitaxial growth on the graphite plate and then stripped away as graphene flakes by the collision force of Ar atoms, which compose the plasma gas. GQDs produced by the injection of ethylene gas at a 2.5 L/min rate were smaller than 20 nm and well-dispersed in common solvents.[41,55] The graphene flakes produced by the injection of ethanol as a carbon source at a 0.1 mL/min rate were very pure and approximately 500 nm in size on average but were not dispersed in common solvents even by sonication.[72] The graphene flakes with a relatively large size were not dispersible, whereas the GQDs with a relatively small size were dispersed but with significantly degraded conductivity due to the quantum confinement effect. To fabricate graphene that can be dispersed in solvents while not significantly degrading its conductivity, the size of graphene should be properly controlled. In the fabrication of graphene using thermal plasma jet, the size of graphene is affected by the injection rate and carbon source.

Herein, we researched the fabrication conditions to fabricate dispersible graphene flakes, not degraded significantly in their conductivity by the quantum confinement effect, using thermal plasma jet. The graphene flakes fabricated using the injection of ethylene gas at a 500 sccm rate were very pure, contained no oxygen, and were few-layered. Although their average size was larger than 100 nm, the flakes were well-dispersed in common

organic solvents by sonication. Furthermore, thin films of the graphene flakes could also be prepared. As a representative application of the films, we fabricated dye-sensitized solar cells (DSSCs) with a graphene flake/FTO counter electrode. The power conversion efficiency was similar to that of a DSSC with a conventional Pt/FTO counter electrode.

1. 4. Onion-type carbon

1. 4. 1. The properties of onion-type carbon and synthetic methods

Onion-type carbon is defined by their structure as spherical or polyhedral carbon nanoparticles, consisting of a number of fullerene-like multiple carbon shells. The onion-type carbon has been shown to be promising new materials in various applications due to the unique multi-shell fullerene structure with nanoscale diameter.[73-78] The onion-type carbon, which was first discovered by Iijima in 1980 and described by Ugarte in 1992, is new additives to a part of carbon materials.[79] Because the onion-type carbon has a small particle size and high electrical conductivity, it can be regarded as final carbon black. The onion-type carbon is mainly prepared by annealing nanodiamond in an inert gas or vacuum at 1200 °C.[74,80,81]

1. 4. 2. Synthetic methods

The onion-type carbon was first obtained by strong electron irradiation of carbon materials. The onion-type carbon has been investigated as being a part of carbon materials, and different

methods for its fabrication has been steadily researched. It is a common method for the preparation of small onion-type carbon, consisting of multiple carbon shells, to use nanodiamond as a starting material under high temperature.[80,81] The nanodiamond can be converted to graphite onion-type carbon by heat treatment or exposure of electron beam. Another method for the onion-type carbon is by arc discharge of graphite in a solution such as liquid nitrogen or water.[82,83] A recent novel method for the preparation of large onion-type carbon is obtained by the use of inorganic starting materials.[84] Large onion-type carbon was fabricated from wood wool as a natural resource, which was pyrolized and treated with concentrated nitric acid.[85] Today, the onion-type carbon can be produced in gram scale amounts by treatment of commercially available nanodiamonds or by combustion of naphthalene.[86] This superior availability of onion-type carbon materials allows for future investigation of the application in various fields.[87-97]

We have researched a novel method to fabricate graphene flakes[72] and GQDs[41,55] using thermal plasma system. In thermal plasma jet, the plasma of Ar was generated by applying a high voltage, and the carbon atomic beam generated by continuous injection of a carbon source into the plasma jet flows through an attached carbon tube (5-20 cm in length), which is attached to the anode. In the fabrication of graphene, a well-poliched graphite plate is placed perpendicularly approximately 10 cm

away from the end of the attached carbon tube while no graphite plate is used to fabricate GQDs. In fabrication of GQDs, the injection rate of a carbon source is much higher than that of graphene flakes. The carbon soot including GQDs is produced by gas collision reaction of high-dencity carbon atomic beam in the attached carbon tube. However, in the produced carbon soot, GQDs based on the amount extracted was about 10%. The remaining was onion-type carbon. (see figure 1.4) This means that mass production of onion-type carbon using thermal plasma jet could be a lower-cost fabrication than the general fabrication method by annealing nanodiamond. The produced onion-type carbon materials need no chemical treatment except for removing GQDs by ethanol. Additionally, our onion-type carbon might have a good crystallinity because as increasing fabrication temperature, the produced carbon materials improve crystallinity. During fabrication of onion-type carbon, temperature of Ar plasma was about 10,000 K.

We have simplified the fabrication of onion-type carbon using a thermal plasma jet and pursued the possibility of treating cancer by photothermal effect. The method for producing onion-type carbon is the same method in the production of GQDs, but GQDs were washed away by a solvent. The average size of onion-type carbon is 15 - 20 nanometers and represents a structure like the cross section of the onion. Onion-type carbon is well dispersed in common solvents and absorbs all light from

ultraviolet to near-infrared (NIR) region. Utilizing this characteristic, it was confirmed that a heat generation was occurred through converting the photo energy into thermal effect after absorption of NIR light. As a representative application, the optical properties of onion-type carbon can be utilized to photothermal therapy (PTT), which ablates abnormal cells such as cancer cells by heat generation after light irradiation using nanoparticles. (see Figure 1.4)

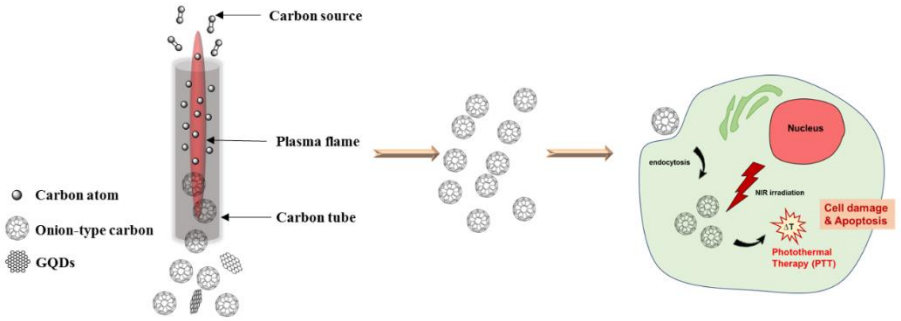

Figure 1. 4. Fabrication of onion-type carbon by gas collision reaction in the attached carbon tube, purification, and photothermal therapy *in vitro*.

Chapter 2

Experimental Section

2. 1. Three kinds of GQDs fabricated by using a thermal plasma jet and PDT *in vitro* and *in vivo*

2. 1. 1. Three kinds of GQDs fabricated by using a thermal plasma jet

Carbon soot including GQDs was fabricated by using a thermal plasma system.[41] A carbon tube (10 cm in length; 1 cm in diameter) was attached to the anode, and thermal plasma of Ar (99.999%, at the injection flow rate of 16.0 L per min) was generated by applying a high voltage of ~3 kV between cathode and anode. The thermal plasma jet for generating a carbon atomic beam was operated by a dc of ~200 A and 60 V. Ethylene gas was inserted continuously (2.5 L per min) as a carbon source into the torch using a gas flow meter (see Figure 2.1a).

For extraction of GQDs, a small amount of the produced carbon soot was scattered carefully on the surface of water that was contained in a vial, and then added cyclohexane carefully to minimize disturbance (see Figure 2.1b). After waiting for 48 h, two layers were separated without including undissolved carbon soot. For a further purification, cyclohexane was added into the separated aqueous phase, while water added into the organic phase. The volume ratio of water and cyclohexane was about 1:1.

GQDs were analyzed by using a high-resolution transmission electron microscope (TEM; JEOL, JEM-3000F (300 kV)). The photoluminescence (PL) and photoluminescence excitation (PLE) spectra were obtained using a homemade spectrophotometer. Absolute quantum yield was measured by absolute PL quantum yield measurement system QE-1200 (OTSUKA Electronics). Atomic force microscopy (AFM) images were taken using a PSIA (XE-150) atomic force microscope. X-Ray Photoelectron Spectroscopy (XPS) analysis was performed using a PHI 5000 VersaProbe^{TM}ULVAC system with an Al Kα X-ray source ($h\nu$ = 1486.6 eV), operated a 15kV and 20 mA beam, and HSA analyzer.

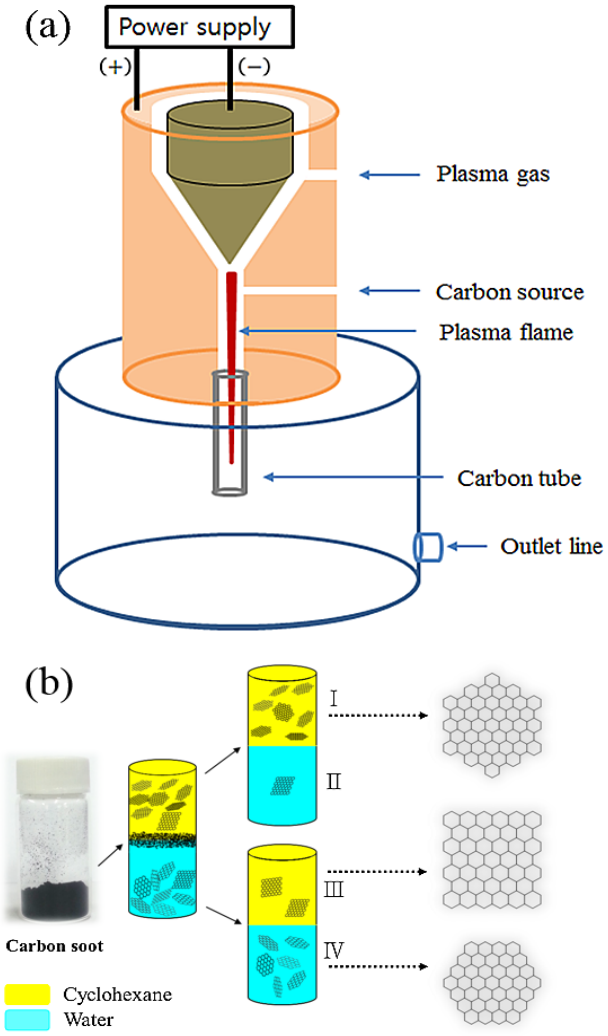

Figure 2. 1. Schematics of (a) the thermal plasma jet system for production of carbon soot and (b) liquid–liquid extraction of three kinds of GQDs from carbon soot produced. Four solutions of I – IV are denoted as cyclohexane/cyclohexane, cyclohexane/water, water/cyclohexane, and water/water solutions, respectively.

2. 1. 2. Zigzag and armchair GQDs for PDT *in vitro and in vivo*

Carbon soot including two kinds of GQDs was fabricated by using a thermal plasma jet. Figure 1.3 represents a schematic of thermal plasma jet and fabrication method. A carbon tube (10 cm in length) was attached to the anode, and thermal plasma of Ar (99.999%, at an injection flow rate of 16.0 L/min) was generated by a high voltage of ~3 kV and a dc of ~200 A at 60 V.[55] Ethylene gas (2.5 L/min) was continuously inserted as a carbon source into the torch (see Figure 2.1). Carbon soot was carefully collected in chamber. Zigzag and armchair GQDs from carbon soot were obtained by liquid–liquid extraction in Figure 1.3.[55] Briefly, a small amount of carbon soot was carefully scattered on the surface of water in a vial, and then added cyclohexane carefully to the vial. After waiting for 48 h, two layers were separated and carried on the different vials. For a further purification, cyclohexane was added into the separated aqueous phase, water, however, added into the organic phase. The solvents of the extracted aqueous and organic phase were allowed to evaperate at 40 °C, and added in anhydrous ethanol. Then zigzag and armchair GQDs solutions were obtained as shown in Figure 2.2. Four miligrams of each zigzag and armchair GQDs were used for bio application. The GQDs was analyzed by

using a high-resolution transmission electron microscope (TEM; JEOL, JEM-3000F (300 kV)). UV/vis spectrum was recorded using a UV-3600 spectrophotometer (Scinco, NEOSYS-2000). The photoluminescence (PL) spectra was analyzed using a homemade spectrophotometer. Atomic force microscopy (AFM) images and analysis were exhibited by a PSIA (XE-150) atomic force microscope. The solution was irradiated with a 365-nm LED laser (Mikwang Electronics, 2 W/cm^2).

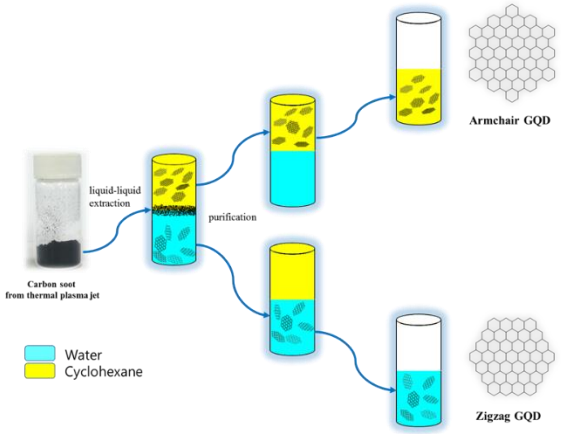

Figure 2. 2. Liquid-liquid extraction of two types of GQDs from carbon soot produced.

Cell culture: Human cervical cancer cell line HeLa and breast cancer cell line MDA-MB-231 were grown in DMEM containing 10% FBS, 1% P/S at 5% CO_2, 37 ° C.

Cellular Toxicity Test: To measure the viability of cells treated

with GQDs, HeLa cells (1×10^4 cells/well) were prepared in a 96-well plate in triplicate for 24 h, followed by incubation with various concentrations of GQDs with complete medium. After 12 h incubation, the cells were then carefully washed with 1x PBS and CCK-8 assay solution was added for 1 h with serum free medium, followed by measuring absorbance at 450 and 670 nm wavelength by using a microplate reader (Molecular Devices, Inc., USA).

Photodynamic therapy *in vitro*: To investigate the therapeutic effect by PDT *in vitro*, GQDs (20 μg/mL) with a serum-free medium was treated with HeLa cells (1.2×10^5 cells/well), which had been pre-incubated in a 12-well plate for 24 h. After the medium exchange to a serum-containing medium, the cells were irradiated with a 365 nm LED (50 mW/cm^2) for 10 sec. After further 12 h incubation, each well was treated with Live/Dead assay reagent based on the manufacturer's protocol. The bright field and fluorescence images of the cells were obtained by using an inverted fluorescence microscope, IX70 (Olympus, Japan) with a 4x objective.

To investigate the quantitative cell viability related to the photodynamic effect of GQDs, HeLa cells (1×10^4 cells/well) were seeded in a 96-well plate, incubated for 24 h, and treated with various concentrations of GQDs. After 12 h incubation, each well was irradiated with a 365 nm LED (50 mW/cm^2) for 10 sec.

After further incubation with serum-containing medium for 12 h, the CCK-8 cell viability assay was performed as described above. All experiments were carried out in triplicate.

Singlet oxygen detection: The SOSG reagent is highly selective to singlet oxygen (SO), and it emits strong green fluorescence in the presence of SO at 530 nm (λ_{ex}= 504 nm). SOSG (5.0 μM) dissolved in 2% methanolic solution was added to GQDs (20 μg/mL). Final volume of each well was 100 μL. The generation of SO was induced by irradiation using a 365 nm light-emitting diode (LED) (50 mW/cm^2). After irradiation, green fluorescence emission from the samples was observed at 530 nm wavelength for 55 min by using a fluorometer.

***In vivo* study:** All animal experiments were carried out in compliance with the Institutional Animal Care and Use Committees (IACUC) of Seoul National University. Balb/c male nude mice (5-weeks old) were purchased from ORIENT BIO, Korea. Tumor-bearing mice were prepared by subcutaneously injecting a suspension of the HeLa cells (6×10^6 cells) in 100 μL of sterilized 1x PBS (n = 4). When the tumor size reached ~50 mm^3, GQDs in 1x PBS solution (20 μm/mL, 100 μL) were injected into the tail veins of the tumor-bearing mice. As a control, one group of mice was treated with the same volume of 1x PBS solution. Bright field and fluorescence images from the

mice were obtained by using an optical molecular imaging system, Optix MX3 (ART, USA) after 24 h of injection. To examine the biodistribution of the injected GQDs, major organs were collected into a petri-dish after 24 h of injection. All acquisition image was operated for pseudo-coloring with fluorescent intensity.

To investigate anti-tumor efficacy, we prepared GQD and 1x PBS as a control in a final volume of 100 μL. Then, the suspensions were injected intravenously after tumor volume of HeLa implanted xenograft mice reached ~50 mm^3, n=4. For the irradiated groups, 365 nm LED (0.5 W/cm^2, 10 sec) was used after 24 h, 5 d, and 10 d of injection. The changes of volume in tumors and body weight were monitored in each group over 2 weeks. The tumor volumes were calculated by using the equation of length × $(width)^2$ × $^1/_2$, where the length and width are the longest and shortest diameters (mm) of the tumor, respectively. The relative tumor volumes were calculated compared to the initial volumes.

Histological Evaluation: Histological specimens were obtained by sacrificing mice following PDT at 14 days of intravenous injection. Samples from the heart, liver, spleen, lung, kidney, and tumor were obtained and placed in 4% PFA solution. The specimens were embedded in Optimal cutting temperature (OCT) compound with sucrose infiltration, sectioned, and processed by using H&E staining (BBC Biochemical, Mt Vernon, WA, USA).

The stained sections were observed under a BX71 microscope with 10x objective lens (Olympus, Tokyo, Japan).

Statistical Analysis: All data shown mean corrected values ± SD of at least four independent experiments. Significant differences were determined based on the Student's t-test performed with GraphPad Software.

2. 2. Fabrication of dispersible graphene flakes using a thermal plasma jet and their thin films for solar cells

A schematic of the thermal plasma jet system is presented in Figure 2.3. Thermal plasma of Ar (99.999%, at an injection flow rate of 16.0 L/min) was generated by applying a high voltage of ~3 kV, and then, the system was operated by applying a dc of ~200 A at 60 V. A carbon tube (20 cm in length; 1 cm in inner diameter) was attached to the anode, and a well-polished graphite plate was placed in the path of the plasma gas flow perpendicular to the attached carbon tube. The distance between the graphite plate and end of the attached carbon tube was 10 cm. Ethylene gas (500 sccm) was continuously inserted as a carbon source into the torch using a mass flow controller. The graphene soot produced was collected from the wall of the thermal plasma

chamber. The graphene flakes (45 mg) were dispersed in 30 mL of organic solvents such as anhydrous ethanol and dimethylformamide (DMF) by sonication for 1 h. Graphene thin films were then prepared using three techniques: electrophoretic deposition, spray-coating, and interfacial assembling and transferring.[97] For electrophoretic deposition, a dc voltage of 40 V was applied between the working and counter electrodes in a dispersed graphene flake ethanol solution (see Figure 2.4). An aluminum or silicon plate was used as the working electrode, and graphite was used as the counter electrode. The gap between the two electrodes was 1 cm. For spray-coating, a graphene suspension in DMF was repeatedly sprayed on FTO glass heated on a hot plate to 80 °C using a portable spray nozzle. For the interfacial assembling and transferring approach, 0.5 mL of a graphene suspension in DMF was mixed with 40 mL of water, and then 4 mL of ethyl acetate (EA) was placed on the surface of the mixture. A self-assembled graphene film on top of the mixture was formed in a few minutes (see Figure 2.5). A graphene flake counter electrode was prepared by transferring the self-assembled graphene film onto FTO glass and then dried at 100 °C for 10 min to remove any residual solvent before annealing at 350 °C for 1 h. A conventional Pt counter electrode was prepared by drop-coating an ethanol solution of H_2PtCl_6 (0.5 mL, 0.5 M) on the clean conductive FTO glass, which was then sintered at 450 °C for 30 min. DSSC devices were fabricated by

following a reported procedure.[98] The graphene flakes were characterized using a scanning electron microscope (SEM; JEOL ltd. JSM6700F (10 kV)) and high-resolution transmission electron microscope (TEM; JEOL, JEM-3000F (300 kV)). UV-vis spectra were recorded using a UV-3600 spectrophotometer (Scinco, NEOSYS-2000). Raman spectra were obtained by excitation with a 514.5-nm laser line using a micro-Raman system equipped with a homemade sample stage, monochromator (SPEX 500 M), and CCD camera cooled with liquid nitrogen (Roger Scientific 7346-001 Model). X-ray photoelectron spectroscopy (XPS) analysis was performed using a ULVAC-PHI 5000 VersaProbe^{TM} system with an Al Kα X-ray source ($h\nu$ = 1486.6 eV) operated at 15 kV and 20 mA. Nuclear magnetic resonance (NMR) spectra were measured using a Varian/Oxford As-500 (500 MHz). The photocurrent density-voltage (J-V) characteristics of the DSSCs were measured using an electrometer (Keithley 2400) under AM 1.5 illumination (100 mW/cm^2) provided by a solar simulator (1-kW xenon with AM 1.5 filter, PEC-L01, Peccel Technologies). The incident photon-to-current conversion efficiency (IPCE) was measured using a McScience model K3100 system with reference to a calibrated diode. A 300-W Xenon lamp was used as a light source, which was coupled to a monochromator. The bias light was supplied by a 150-W halogen lamp. Cyclic voltammetry (CV) was performed on a CHI600E electrochemical analyzer (CH

Instruments) in an acetonitrile solution containing 0.1 M $LiClO_4$,10 mM LiI,and 1 mM I_2 at room temperature under an inert atmosphere of Ar, equipped with a platinum wire counter electrode and $Ag/AgNO_3$ (0.1 M) reference electrode. Graphene and Pt electrodes were used as the working electrode.

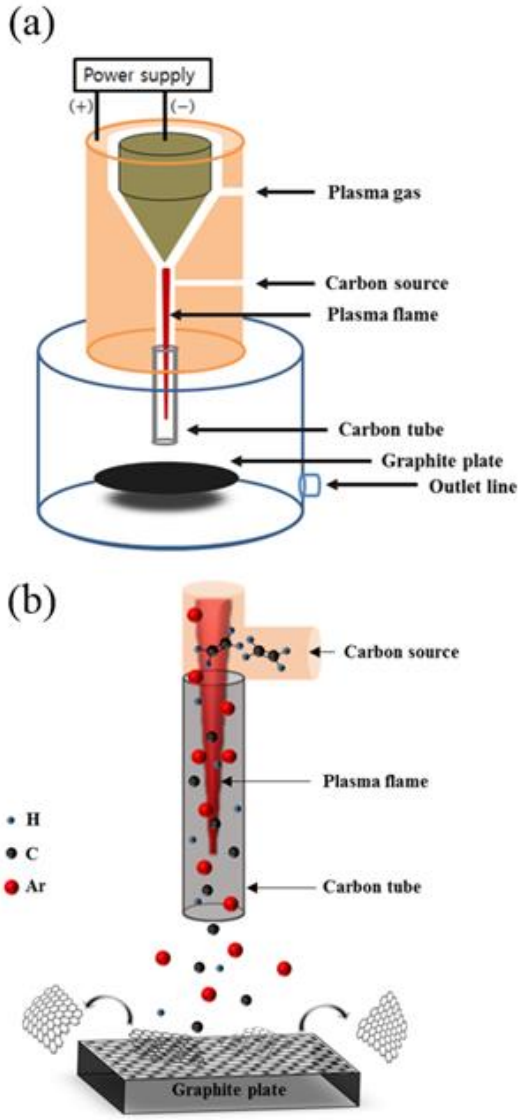

Figure 2. 3. Schematics of the (a) thermal plasma jet system and (b) growth and stripping away of graphene flakes by the collision of an atomic beam on the graphite plate placed at the front of the attached carbon tube.

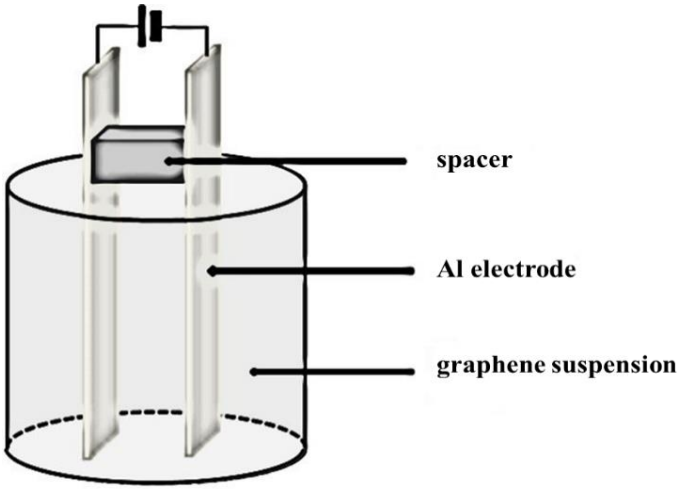

Figure 2. 4. Schematic of the electrophoretic deposition step. The spacer was 1 cm in length. In deposition, a DC 40 V was applied for 7 min.

Figure 2. 5. Time-lapse photographs of graphene assembly at a

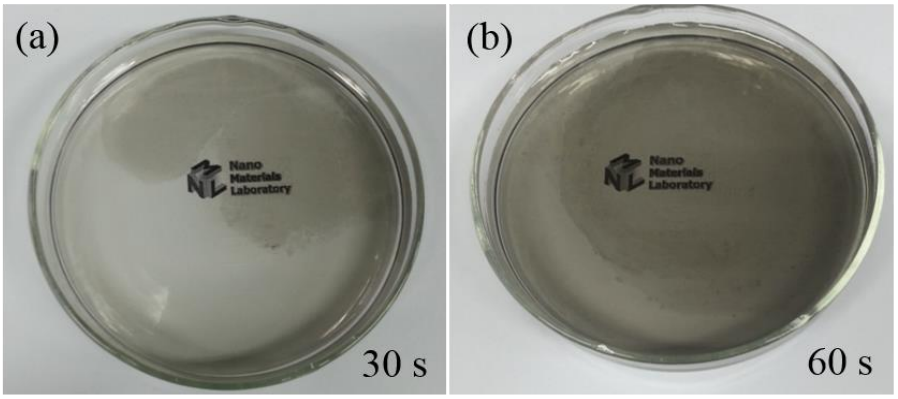

liquid surface. The samples were prepared by using the technique of interfacial assembling.

2. 3. Fabrication of onion-type carbon using thermal plasma jet and photothermal therapy

Carbon soot including onion-type carbon was fabricated by using a thermal plasma jet. A schematic of thermal plasma jet is presented in Figure 2.6. A carbon tube (10 cm in length) was attached to the anode, and the plasma of Ar (99.999%, at an injection flow rate of 16.0 L/min) was generated by a high voltage of ~3 kV and a dc of ~200 A at 60 V. Ethylene gas (2.5 L/min) was continuously inserted as a carbon source into the torch using a gas flow meter. Carbon soot solution including GQDs and onion-type carbon in ethanol were filtered by paper. Then onion-type carbon materials without GQDs were obtained. Onion-type carbon was analyzed by using a high-resolution transmission electron microscope (TEM; JEOL, JEM-3000F (300 kV)). UV/vis spectrum was recorded using a UV-3600 spectrophotometer (Scinco, NEOSYS-2000). The solution was irradiated with a 808-nm LED laser (Mikwang Electronics, 2 W/cm^2).

Cell culture: Human cervical cell line (HeLa cells) was grown in DMEM containing 4.5 g/L D-glucose containing 10% FBS, 1% penicillin and streptomycin at 5% CO_2, 37 °C.

Cellular Toxicity Test: To investigate the cytotoxicity of onion-type carbon, HeLa cells were seeded 5 x10^3 in a 96-well plate for 24 h, and onion-type carbon was treated with the HeLa cells at varying concentrations (0-500 μg/mL) in serum-containing media. After 12 and 24 h incubation, the cells were carefully washed with 1× PBS twice and replaced in fresh medium; then, CCK-8 assay solution was added, incubation was carried out for 1 h, and the absorbance at 450 was measured by using a microplate reader (Molecular Devices, Inc., USA).

Photothermal therapy *in vitro*: To investigate the therapeutic effect by photothermal therapy *in vitro*, onion-type carbon (50 μg/mL) with a serum-free medium was treated with HeLa cells (1.2 × 10^5 cells/well), which had been pre-incubated in a 12-well plate for 24 h. After the medium exchange to a serum-containing medium, the cells were irradiated with a 808 nm laser (2 W/cm^2) for 10 min. After further 12 h incubation, each well was treated with Live/Dead assay reagent based on the manufacturer's protocol. The bright field and fluorescence images of the cells were obtained by using an inverted fluorescence microscope, IX70 (Olympus, Japan) with a 4x objective.

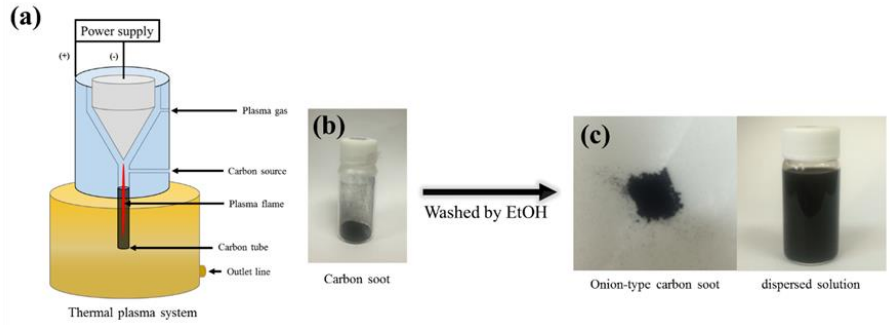

Figure 2. 6. (a) Thermal plasma system, (b) the produced carbon soot, (c) onion-type carbon and dispersed suspersion.

Chapter 3

Three types of GQDs fabricated using thermal plasma jet: characteristics of dots determined by edge structure

3. 1. Characteristics of GQDs determined by edge structures

Figure 3.1. shows the low (a-c) and high (d-f) resolution TEM images of GQDs and (g) the fast Fourier transform (FFT) pattern of a GQD. GQDs were extracted from the carbon soot produced using the liquid-liquid extraction method. Water and cyclohexane were used as polar and nonpolar solvents, respectively. It should be mentioned that the dominant species in carbon soot is the onion−type carbon material, which does not disperse without sonication. Four solutions containing GQDs were denoted as cyclohexane/cyclohexane, cyclohexane/water, water/ cyclohexane, and water/water solutions (see Figure 2.1b). The GQDs included in the cyclohexane/cyclohexane solution could be dissolved favorably in a nonpolar solvent, while those included in the water/water solution dissolved favorably in a polar solvent. GQDs included in the solutions of cyclohexane/water or water/cyclohexane solution could be dissolved in both polar and nonpolar solvents. In the cyclohexane/water solution, we could not observe GQDs due to very low concentration even though the solution showed very weak fluorescence. GQDs shown in Figure 3.1a were obtained from the cyclohexane/cyclohexane solution. Their average size is about 13 nm (see Figure 3.2). Although the corners are not

well developed, one can clearly see sides from all GQDs. They have basic hexagonal shapes (see Figure 3.5). GQDs shown in Figure 3.1b have been obtained from the water/water solution. The average size is about 11 nm (see Figure 3.3). They also have basically hexagonal shapes (see Figure 3.5). Some look like circular. This may be due to the fact that hexagonal shapes seem to be seen as circular shapes when the corners are not well developed. It should be mentioned that GQDs were made by collisions of carbon atoms. Therefore, the corners could not be made clearly as shown in Figure 1.1. GQDs shown in Figure 3.1c have rectangular shapes. They have been obtained from the water/cyclohexane solution. Their shape is relatively uniform as squares but their size has a large distribution. The largest one was about 300 nm, while the smallest one was about 15 nm. The large ones may be too big to be called as GQDs. The average size is about 53 nm (see Figure 3.4). It should be mentioned that the average of GQDs could be controlled by varying the length of carbon tube attached to anode. It is known that the average size of GQDs increases with increasing the length of carbon tube attached to anode. In high-resolution TEM images of three kinds of GQDs, uniform lattice fringes are clearly seen. By AFM analysis, three kinds of GQDs are all single-layered. The height profiles of the lines in Figure 3.6-8 show that the thickness of the GQDs is less than 1 nm, which is in good agreement with the reported value for single-layered graphene. The corresponding

the FFT patterns of GQDs are shown in Figure 3.1g and 3.9−11. They show a hexagonal pattern without any satellite spots. XPS was performed to determine the composition of three kinds of GQDs (see Figure 3.12). The measured spectra could be deconvoluted into four surface components, corresponding to sp^2 (C=C) at binding energy of 284.5 eV, sp^3 (C−C, and C−H) at 285.5 eV, C−OH at 286.6 eV, as well as O=C−OH at 288.6 eV. The bands corresponding to C−OH and O=C−OH were relatively weak. In principle, oxygen is not contained in our fabrication, since only Ar and ethylene gases have been added into a plasma system as the plasma gas and carbon source, respectively. Therefore, oxygen of the hydroxyl and carboxyl groups might be included during the preparation process of XPS samples. It should be mentioned that H termination could take place because hydrogen atoms generated is twice of carbon atoms when ethylene molecules are decomposed. However, we could not get any information to be helpful in explaining the polar or nonpolar characters of GQDs or evidence of the H termination from the analysis of XPS or Raman spectra. This may be due to that the number of edge carbon or hydrogen atoms is relatively very small compared to the total number of carbon atoms of GQDs. The shape and dissolving property of our three kinds of GQDs are well agreed with those predicted from the model GQDs (see Figure 1.1). Therefore, it is concluded that GQDs obtained from the cyclohexane/cyclohexane solution are armchair (or nonpolar

hexagonal) GQDs having carbyne edges. GQDs obtained from the water/water solution are zigzag (or polar hexagonal) GQDs having carbene edges. GQDs obtained from the water/cyclohexane solution are hybrid (or amphoteric rectangular) GQDs having carbyne and carbene edges in each dot. Our conclusion is supported by the PL and PLE data. It is known that the PL of GQDs is determined by the edge structures.[40] Hybrid GQDs have both carbyne and carbene edges in each dot. Therefore, the PL spectra of hybrid GQDs may show the characteristic peaks corresponding to both armchair and zigzag GQDs. The PL and PLE spectra of three kinds of GQDs are shown in Figures 3.13 and 3.14, respectively. [The UV−vis absorption spectra of armchair, zigzag, and hybrid GQD suspensions in ethanol are shown in Figure 3.15. Additional PL spectra are shown in Figure 3.15. with the luminescence pictures of GQD suspensions taken under 365 nm UV light.] In general shapes, the PL spectra of the hybrid (or amphoteric) GQDs seem to be the combination of the spectra of armchair (or nonpolar) and zigzag (or polar) hexagonal GQDs. A similar behavior is also observed in the PLE spectra. In the hybrid GQDs, the carbyne and carbene edges are not contacted directly except at four corners. It is known that the zigzag and armchair edges of graphene show different electronic and optical properties.[99,100] Therefore, one could assume that the carbyne and carbene edges of the hybrid GQDs do not affect strongly each other. If this

assumption is true, the frequency of the peaks of hybrid GQDs should be matched to either that of zigzag or armchair GQDs and the intensity may simply correspond to the intensity sum of armchair and zigzag GQDs. However, the relative intensity of some PL and PLE peaks of hybrid GQDs is significantly different from that of zigzag or armchair GQDs. For example, the PL spectrum measured by excitation with 318 or 325 nm is very strong for zigzag GQDs but medium for hybrid GQDs. For the PL spectrum measured by excitation with 403 nm light is very strong for armchair GQDs, while weak for hybrid GQDs. For the PLE spectrum measured by monitoring at 378 nm is very strong for zigzag GQDs, while medium for hybrid GQDs. In the PLE spectrum measured by monitoring at 460 nm, the peaks at 403 and 425 nm are strong for armchair GQDs, while those are weak for hybrid GQDs. The frequency of the PL peaks of hybrid GQDs is well matched to either that of zigzag or armchair GQDs. The peak near 410 nm, whose λ_{max} is slightly different in each spectrum, of hybrid GQDs could be due to two close peaks at 412 nm for zigzag GQDs and at 408 nm for armchair GQDs. For the PLE spectra, several discrepancies in frequency are clearly observed. For example, for the PLE spectra measured by monitoring at 327 nm (3.79 eV), the strongest peak is at 291 nm (4.26 eV) for zigzag GQDs, while at 285 nm (4.35 eV) for hybrid GQDs. The λ_{max} is blue shifted from 291 to 285 nm. A similar shift, from 296 nm (4.19 eV) to 291 nm (4.26 eV), is observed

in the PLE spectra measured by monitoring at 342 nm (3.64 eV). The strong PLE peaks near 372 nm (3.33 eV) of hybrid GQDs are not matched to any peak of armchair or zigzag GQDs. The λ_{max} is slightly shifted when the monitoring wavelength is changed. These peaks could be due to two peaks of armchair GQDs at 363 nm (3.42 eV) and 381 nm (3.25 eV). The former is weak, while the latter is relatively strong. The wavelength of 372 nm (3.33 eV) is corresponding to the middle of these two peaks in energy. Therefore, the peaks near 372 nm could be due to the two peaks at 363 and 381 nm, whose intensities were very similar to each other. The slightly different wavelength may be due to the factor that the λ_{max} is shifted toward the stronger peak when the relative intensity of the two peaks is not equal. From our observations, it is concluded that the relative intensity of some PL and PLE peaks of hybrid GQDs is significantly different from that of armchair or zigzag GQDs. However, the frequency of the PL peaks is well matched to that of zigzag or armchair GQDs. For some PLE peaks, the frequency corresponding to roughly the vibrational energy of the excited state is shifted. By the theoretical calculation, there are seven energy levels for both carbyne and carbene, and the HOMO level is singlet for carbyne, while triplet for carbene. The peak intensity is determined by the vibrational overlap integral.[101,102] By the Frank–Condon principle, the vibrational overlap integral could be changed when the upper or ground potential curve is displaced. When the potential curve

is displaced, the absorption frequency is also changed in a vertical transition. Since no significant discrepancy in the PL frequency is observed, it is concluded that the electronic structure of armchair edges of hybrid GQDs is very similar to that of armchair GQDs and that of zigzag edges to that of zigzag GQDs. To show some significant discrepancy in relative intensity, the potential curves of hybrid GQDs should be slightly displaced from those of armchair or zigzag GQDs. Hybrid GQDs have both carbyne and carbene edges in each dot. Two unshared valence electrons exist at each carbon atom of zigzag edges, while carbon triple bonds exist at armchair edges. The former could act like electron donors and the latter as electron acceptors. Therefore, they could affect each other even though they are not contacted directly except four corners. This should be studied in detail. The absolute quantum yields of armchair, zigzag and hybrid GQDs are summarized in Table 1. The quantum yield of hybrid GQDs is relatively very high as 25.3%. That of zigzag GQDs is 10.8%, which is the lowest. The PL intensity of zigzag GQDs is the highest when they are excited by a light of 300 nm (see Figure 3.13a). Due to limited light sources, the quantum yield of zigzag GQDs was measured by excitation with a 360 nm light. However, we could roughly figure out the actual quantum yield of zigzag GQDs. In the PL spectra of hybrid GQDs (see Figure 3.13c), the intensity is slightly higher at high energy region than low energy region. The high energy region is mainly contributed

by carbene edges. This may mean that the quantum yield of zigzag GQDs having carbene edges is slightly higher than that of armchair GQDs having carbyne edges. Therefore, the actual quantum yield of zigzag GQDs might be higher than 17.4% of armchair GQDs. It is known that the quantum yield of GQDs decreases with increasing average size, while the PL and PLE spectra not change.[41]

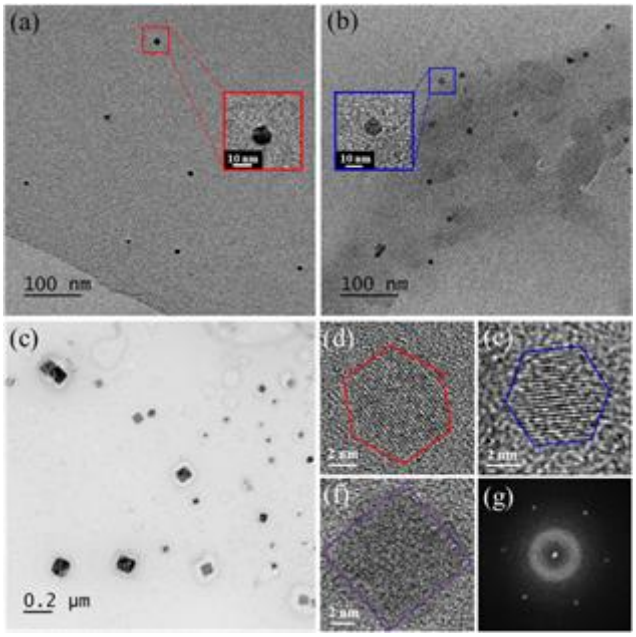

Figure 3. 1. Low- and high-resolution TEM images of (a, d) armchair (or nonpolar hexagonal), (b, e) zigzag (or polar hexagonal) and (c, f) hybrid (or amphoteric rectangular) GQDs, and (g) the 2D FFT pattern of a zigzag GQD.

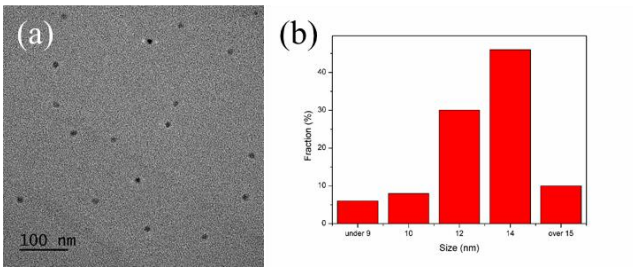

Figure 3. 2. (a) A low-resolution TEM image and (b) size distribution histogram of armchair GQDs. The average size is about 13 nm.

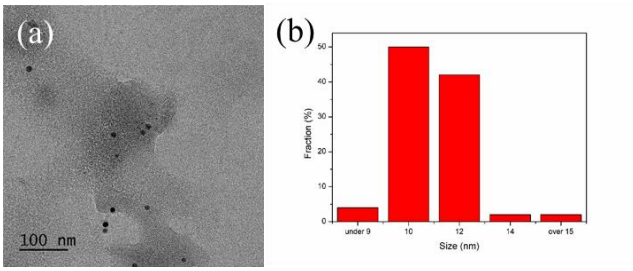

Figure 3. 3. (a) A low-resolution TEM image and (b) size distribution histogram of zigzag GQDs. The average size is about 11 nm.

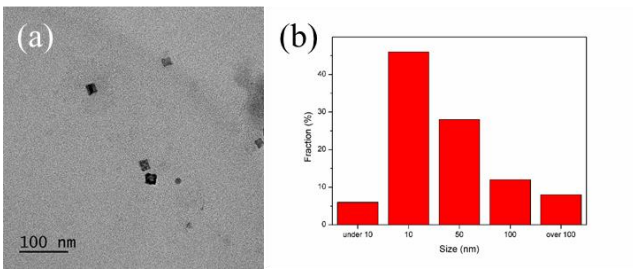

Figure 3. 4. (a) A low-resolution TEM image and (b) size distribution histogram of hybrid GQDs. The average size is about 53 nm.

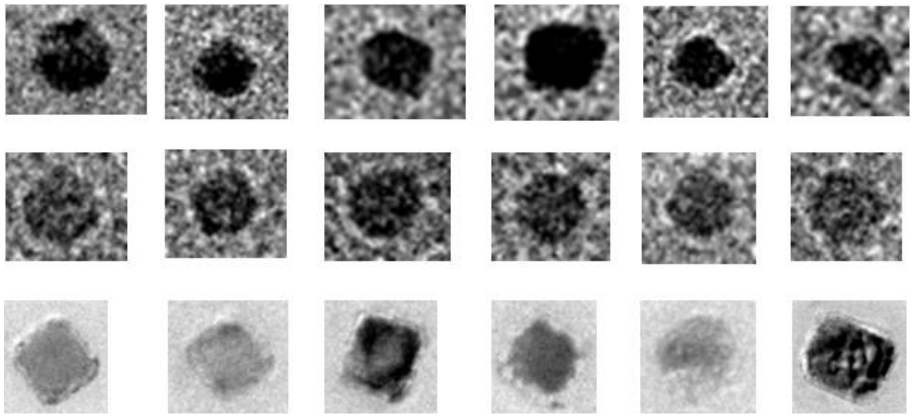

Figure 3. 5. Shapes of (top row) armchair, (middle row) zigzag, and (bottom row) hybrid GQDs.

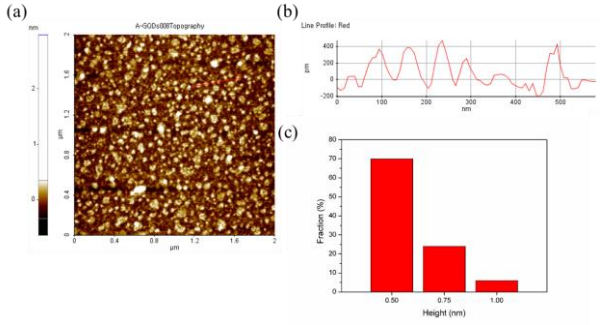

Figure 3. 6. AFM image (a), height profile (b), and height distribution histogram (c) of armchair GQDs.

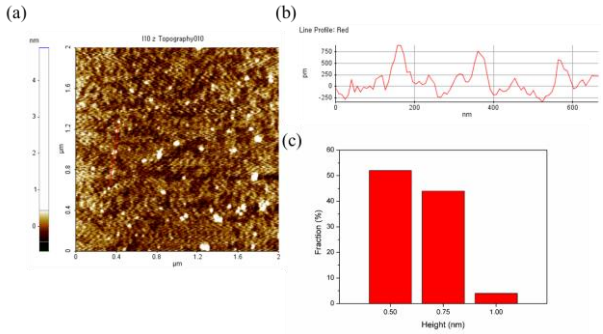

Figure 3. 7. AFM image (a), height profile (b), and height distribution histogram (c) of zigzag GQDs.

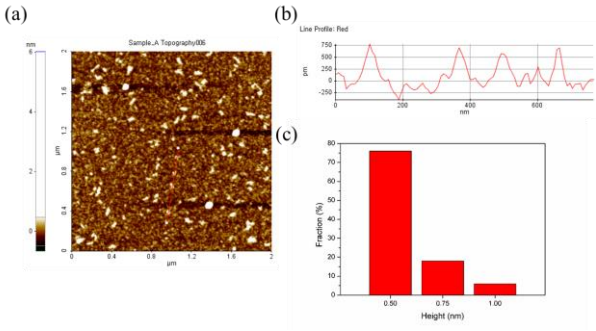

Figure 3. 8. AFM image (a), height profile (b), and height distribution histogram (c) of hybrid GQDs.

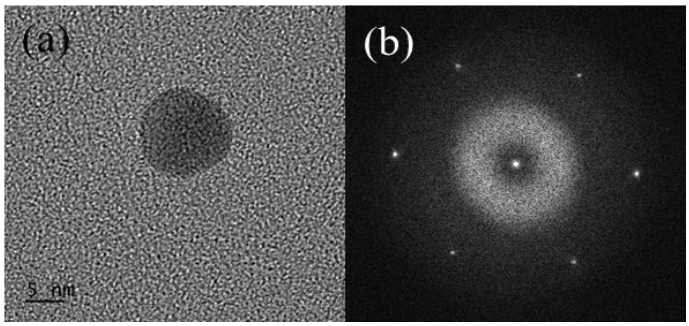

Figure 3. 9. HRTEM image (a) and the 2D FFT pattern (b) of an armchair GQD.

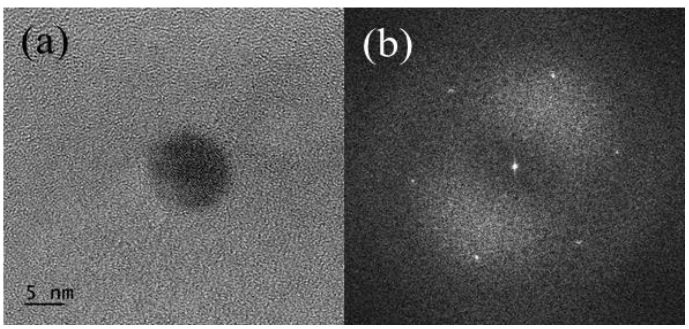

Figure 3. 10. HRTEM image (a) and the 2D FFT pattern (b) of a zigzag GQD.

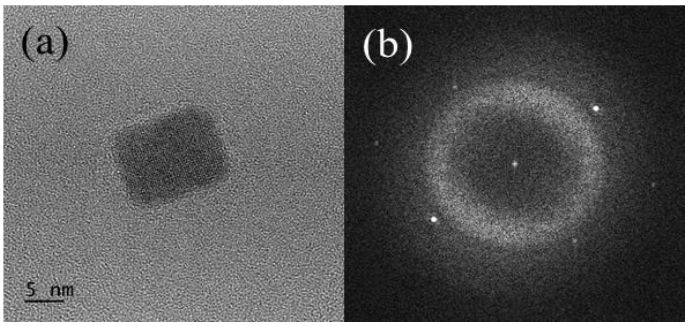

Figure 3. 11. HRTEM image (a) and the 2D FFT pattern (b) of a hybrid GQD.

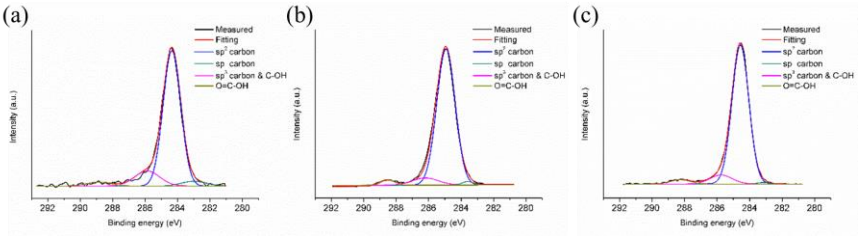

Figure 3. 12. XPS C 1s spectra of (a) armchair, (b) zigzag, and (c) hybrid GQDs.

For a 2.5 L min−1 injection rate of ethylene gas, the production rate of carbon soot is 40 g/h.[41] GQDs are about 10% of the carbon soot produced, and the production rate of GQDs is about 4 g/hour.[41] We estimated the relative abundance of three kinds of GQDs by comparing their relative PL intensities. For measuring the PL spectra, the extracted solution of armchair GQDs was diluted 5 times, while the extracted solution of zigzag and hybrid GQDs was concentrated 4 times. To simplify, the quantum yield of three kinds GQDs was assumed to be equal. The relative

abundance of armchair, zigzag and hybrid GQDs was calculated as 96.9, 2.7, and 0.4%, respectively. Hybrid (or amphoteric rectangular) GQDs have carbyne and carbene edges in each dot. The shape of our hybrid GQDs is very uniform as squares (see Figure 3.1). Since it is known that the PL of GQDs is determined by the edge structures,[1,40] the PL and PLE spectra of hybrid GQDs will respond to the combination of the spectra of zigzag and armchair GQDs. This is well agreed with our observations (see Figures 3.13 and 3.14). By model GQDs shown in Figure 1.1, an armchair GQD has only carbyne edges, while a zigzag GQD only carbene edges. The shape of armchair and zigzag GQDs is not uniform (see Figures 3.1 and 3.5). If carbene edges are partially formed in armchair GQDs or carbyne edges in zigzag GQDs, the peaks corresponding to minority should be observed. Nevertheless, they are not found in the PL and PLE spectra of armchair and zigzag GQDs (see Figures 3.13 and 3.14). This may mean that even though their shapes are not perfectly hexagonal, zigzag GQDs have only carbene edges and armchair GQDs have only carbyne edges. This could be possible only when the characteristics of edges do not change during growth of GQDs. Therefore, it is concluded that the seeds having both carbene and carbyne edges grow as hybrid GQDs, while the seeds having only carbene or carbyne edges grow as zigzag or armchair GQDs, respectively. Under our experimental conditions, it is very hard to collect the seeds of GQDs, because they could flow out of the

chamber with Ar gas, which is the plasma gas, during fabrication. The growth mechanism of seeds should be studied in detail.

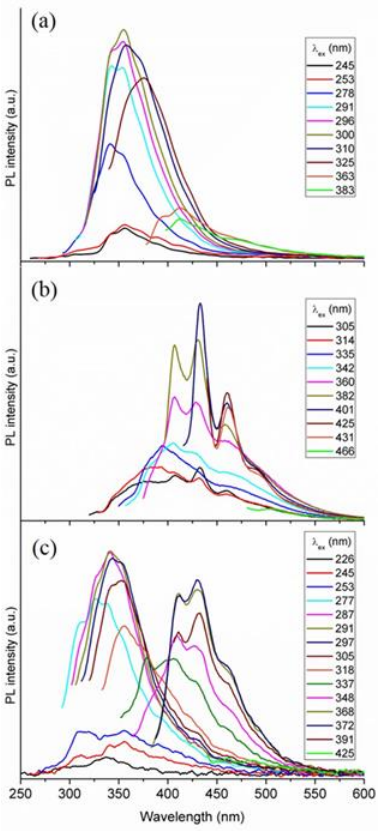

Figure 3. 13. PL spectra of (a) zigzag (or polar hexagonal), (b) armchair (or nonpolar hexagonal), and (c) hybrid (or amphoteric rectangular) GQDs. Ethanol was the solvent for all samples. The legends are the excitation wavelengths.

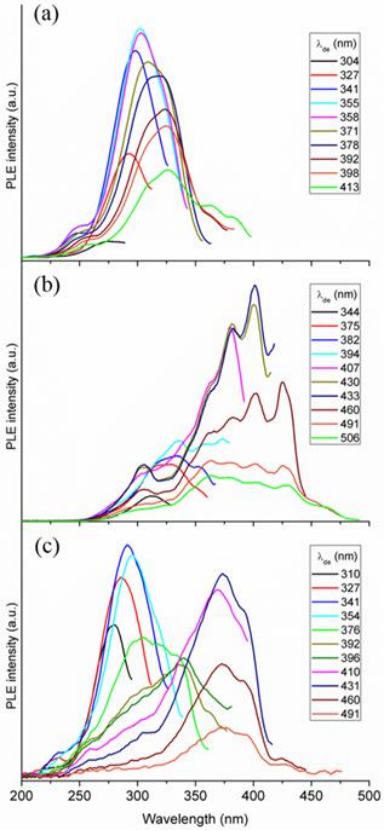

Figure 3. 14. PLE spectra of (a) zigzag (or polar hexagonal), (b) armchair (or nonpolar hexagonal), and (c) hybrid (or amphoteric rectangular) GQDs. Ethanol was the solvent for all samples. The legends are the detection wavelengths.

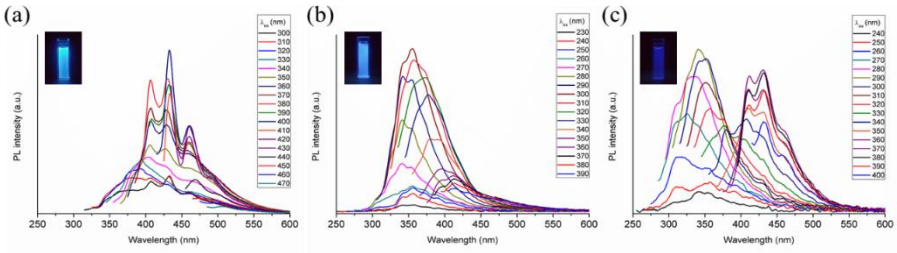

Figure 3. 15. PL spectra of (a) armchair, (b) zigzag, and (c) hybrid GQD suspensions in ethanol with varying the excitation wavelength (λ_{ex}). The luminescence picture of each kind of GQD suspension taken under 365 nm UV light is inserted.

Table 3. 1. Absolute quantum yields of three types of GQDs

Types of graphene quantum dots	λ_{ex} (nm)	Absorbance of the GQD solution	Quantum yield (QY)
Armchair GQDs	370	0.05	15.6%
	400	0.05	17.4%
Zigzag GQDs	360	0.05	10.8%
	370	0.05	8.6%
Hybrid GQDs	360	0.05	23.7%
	370	0.045	25.3%
9,10-Diphenylanthracene (blue dye)	370	0.05	91.3%

In conclusion, We have fabricated three kinds of GQDs by a gas phase collision reaction of carbon atoms using a thermal plasma jet. They were extracted, using liquid−liquid extraction method, from carbon soot produced. Their shapes, dissolving properties in polar and nonpolar solvents, and PL data are well agreed with the three model GQDs, which are made when a graphene sheet is tailored along the zigzag or armchair lines. Armchair (or nonpolar hexagonal) GQDs, having carbyne edges,

are well dispersed in nonpolar solvents like cyclohexane and have basically hexagonal shapes. Zigzag (or polar hexagonal) GQDs, having carbene edges, are well dispersed in polar solvents like water and have basically hexagonal shapes. Hybrid (or amphoteric GQDs are well dispersed in both polar and nonpolar solvents and have rectangular shapes. They have both carbyne and carbene edges in each dot. The PL and PLE spectra of hybrid GQDs contained almost all peaks of the armchair and zigzag GQDs. The absolute quantum yields of three kinds of GQDs are relatively very high. Hybrid GQDs show the highest yield of 25.3%. For a 2.5 L/min injection rate of ethylene gas, the production rate of GQDs is about 4 g/hour. The relative abundance of armchair, zigzag and hybrid GQDs is 96.9, 2.7, and 0.4%, respectively.

3. 2. Photo-induced reactive oxygen species generation upon edge type of graphene quantum dot for enhanced photodynamic therapy *in vitro* and *in vivo*

Two types of GQDs were fabricated using the thermal plasma jet. The produced carbon soot contains onion-type carbon and GQDs. The GQDs, including zigzag and armchair GQDs, were separated by a liquid-liquid extraction method.[55] Water was used as a polar solvent and cyclohexane was used as a nonpolar solvent. Graphene of zigzag structures has two unshare valence electrons with relatively polar property, while graphene of armchair structures has triple bonds with nonpolar property. Thus, zigzag GQDs move to water solvent and armchair GQDs move to cyclohexane solvent. Two types of GQDs are theoretically known as other properties. Experimentally, two types of GQDs showed other properties.[55] In Figure 3.16, two types of GQDs is seen. Figure 3.16a demonstrates a TEM image of armchair GQDs and Figure 3.16b describes a TEM image of zigzag GQDs. They exhibit the basic hexagonal shapes. The average size of armchair GQDs was about 13 nm while that of zigzag was about 11 nm.[55] Figure 3.17-18 implies the characteristics of both GQDs. We confirmed that the thickness of two GQDs is under 1 nm, and

their the peak of sp^2 carbon in the XPS analysis appears to be very strong in both GQDs. In PL spectra, however, the two quantum dots have different characteristics. In the case of zigzag GQDs, very strong peak indicates at the exciation wavelength of 300 nm, while armchiar GQDs displays very strong peaks at the excitation wavelength of 400 nm, which presents that two types of GQDs have other optical properties. In this experiment, we used 365 nm light in PDT. Although two types of GQDs have PL peaks at 365 nm, the difference of UV/vis absorption and PL intensity prove that two quantum dots have other optical properties. We study therapeutic effect of the edge structures, having different properties, by performing PDT experiments using two types of GQDs.

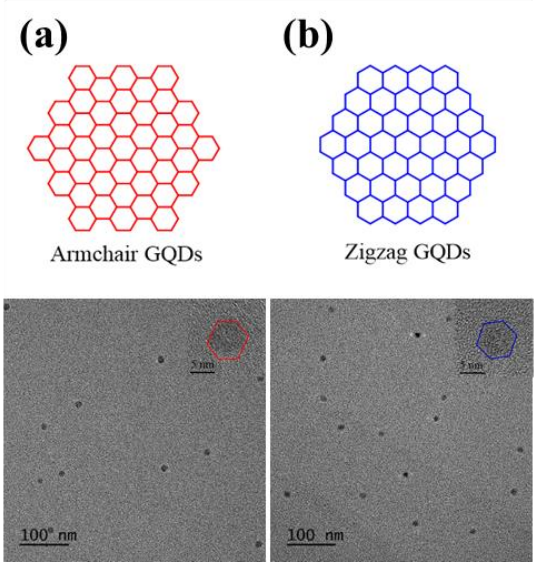

Figure 3. 16. The edge structures of GQD. (a) A model of armchair GQDs and TEM images of armchair GQDs, (b) A model of zigzag GQDs and TEM images of zigzag GQDs

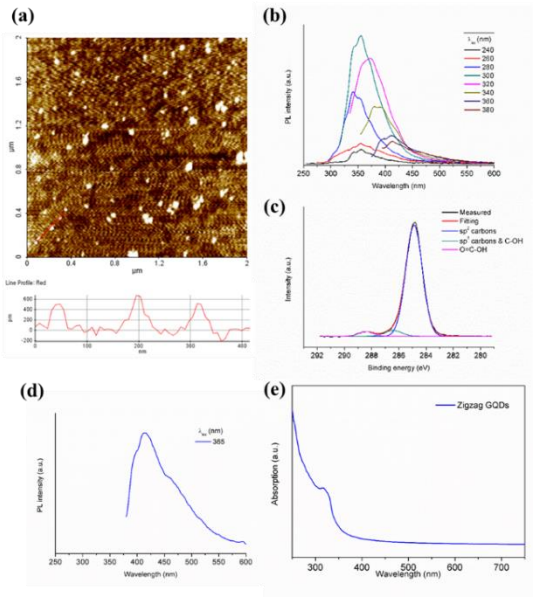

Figure 3. 17. Characterization of zigzig GQD. (a) AFM image with line profile, (b) PL spectra, (c) XPS analysis, (d) PL spectrum of excitaion at 365 nm, and (e) UV/vis spectra.

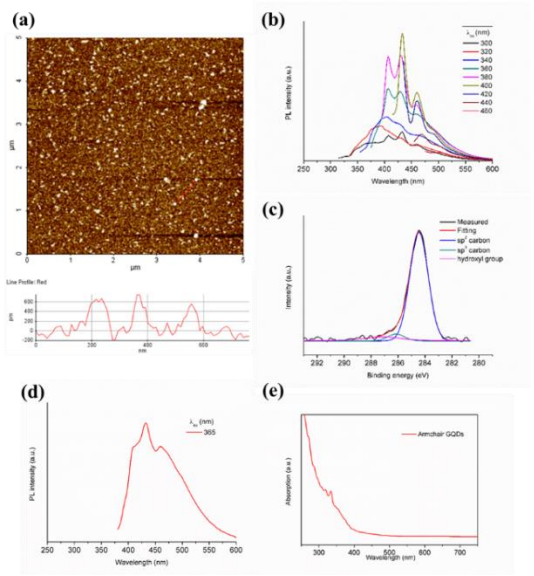

Figure 3. 18. Characterization of armchair GQD. (a) AFM image with line profile, (b) PL spectra, (c) XPS analysis, (d) PL spectrum of excitaion at 365 nm, and (e) UV/vis spectra.

231 cells which are a human cervical cancer cells and breast cancer cells, respectively. After confirming that the treatment of GQDs (up to ~25 μg/mL) to HeLa cells hardly decreased cell viability (see Figure 3.19), we evaluated the intracellular localization of armchair GQDs and zigzag GQDs by monitoring the blue and green fluorescence at 461 nm (λ_{ex}=365 nm) and 520 nm (λ_{ex}=497 nm), respectively. As shown in Figure 3.20, intense both blue and green fluorescence of armchair GQDs appeared in the cytoplasm of the cells. In contrast, no notable fluorescence was shown in zigzag GQDs treated cells, suggesting the two possibilities of the cellular uptake capability and the reactivity against the light activation. Even though both particles internalized the cells through the possible cellular uptake pathway such as clathrin or caveolae-mediated endocytosis, the uptaken armchair GQDs were activated by proper energy sources in the range of UV-vis wavelength only, which is well described in Figure 3.18.

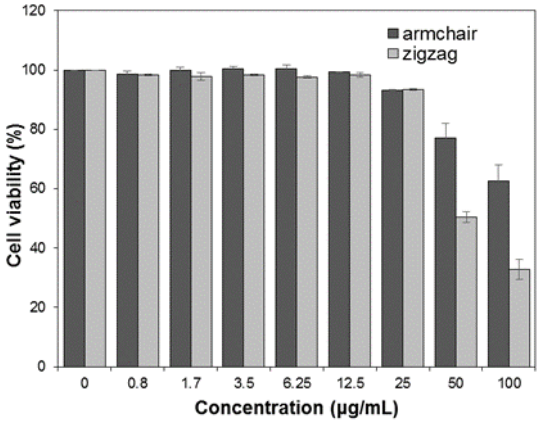

Figure 3. 19. Cell viability of HeLa cells was measured with various concentration after treatment of GQDs for 12 h by cell viability assay kit.

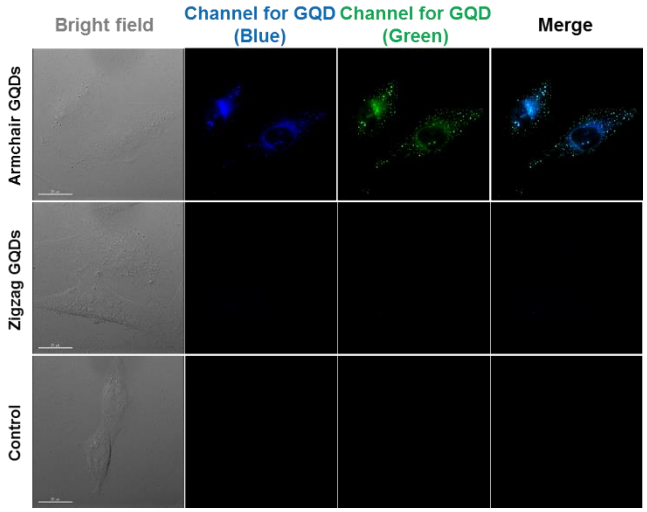

Figure 3. 20. Intracellular uptake study of armchair GQD. Fluorescence of GQD was monitored in MDA-MB-231 cells. Blue (λ_{ex} = 365 nm) and green (λ_{ex} = 475 nm) fluorescence signal were strongly observed in armchair GQD treated cells.

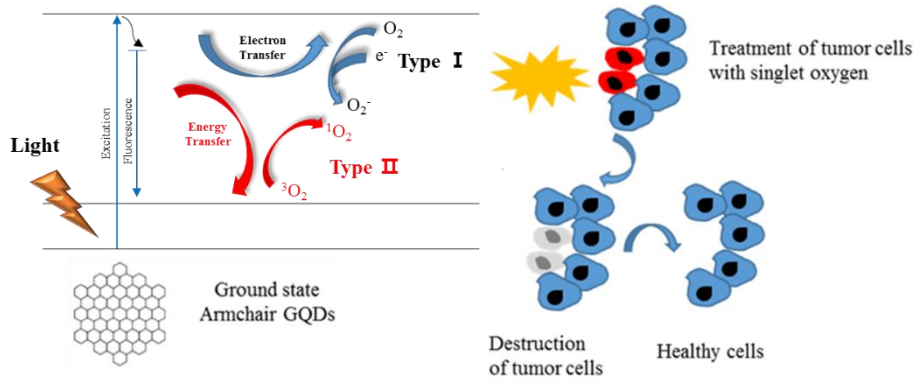

Figure 3. 21. Type I and type Ⅱ reaction of PDT using armchair GQDs.

The PDT is typically generated by Type Ⅰ and Type Ⅱ. Type Ⅰ process involves in a reaction of singlet or triplet photosensitizer, while Type Ⅱ process involves oxygen molecule of excited triplet photosensitizer. In PDT experiment, armchair GQDs have effect on both types (See Figure 3.21). We confirmed the photodynamic effects of armchair structures through several experiments. Two experiments were performed using two types of GQDs. Oxygen gas was injected into solutions of armchair and zigzag GQDs to artificially generate ROS in order to support Type Ⅱ. Figure 3.22-23 is the result of PL measurement after fusing oxygen gas for 24 hours. PL intensities of armchair GQDs decreases in Figure 3.22. In addition, when using the excitation light at 365 nm after oxygen fusing, PL intensity was remarkably decreased as compared with the previous solution, non-fusing oxygen gas (see Figure 3.23). On the other hand, PL intensities

of zigzag GQDs after fusing oxygen gas for 24 hours have no change as shown in Figure 3.22. It can be indirectly confirmed that armchair GQDs generate ROS only, while zigzag GQDs generate non-ROS. As a result, it is supporting that cancer cells are destroyed by armchair GQDs. Methylene blue solution was used to confirm the photocatalytic phenomenon as supporting Type Ⅰ. Photocatalyst is a reaction to decompose the ionic and molecular species by strong reduction or oxidization of negatively charged electrons from a semiconductive material when irradiating light over the bandgap energy. It is possble to convert harmful organic substances to carbon dioxide and water. The reduction reaction makes also it possible to reduce or to separate heavy metal in aqueous solution. The strong oxidation reaction of the photocatalyst can change the color of the methylene blue solution only by exposure of light at room temperature. It can confirm the movement of electrons in armchair GQDs solution when changing the color of methylene blue. In Figure 3.24a, when armchair GQDs solution was mixed with methylene blue and irradiated with light, the peak at 668 nm became lower as increasing time, which means that the electrons of armchair GQDs moved to methylene blue, then the color changed due to the oxidation reaction of methylene blue. Therefore, it is possible to indirectly confirm Type Ⅰ process of armchair GQDs.

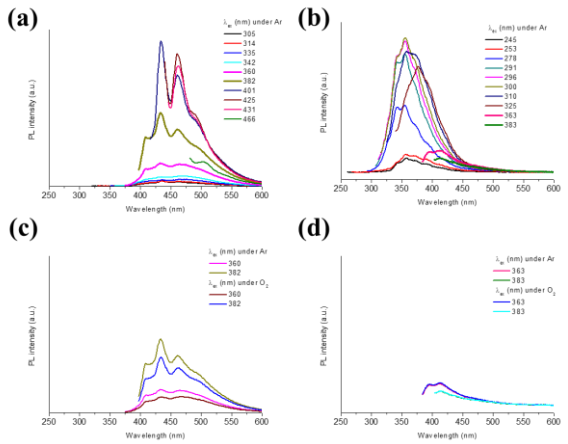

Figure 3. 22. PL spectra of GQD derivatives under Ar and Ar/O_2. (a–b) (top panel) PL spectra under Ar condition. (a) armchair, and (b) zigzag GQD. (c–d) (bottom panel) PL spectra uner Ar/O_2 condition (c) armchair and (d) zigzag GQD.

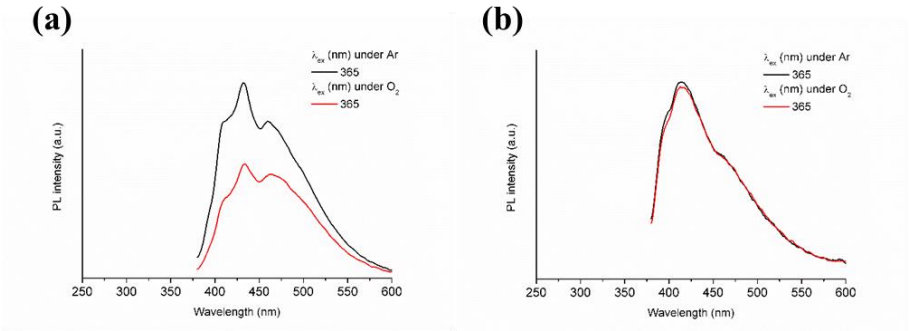

Figure 3. 23. PL spectra of GQD derivatives under Ar/O_2 (λ_{ex}=365 nm). (a) armchair and (b) zigzag GQDs

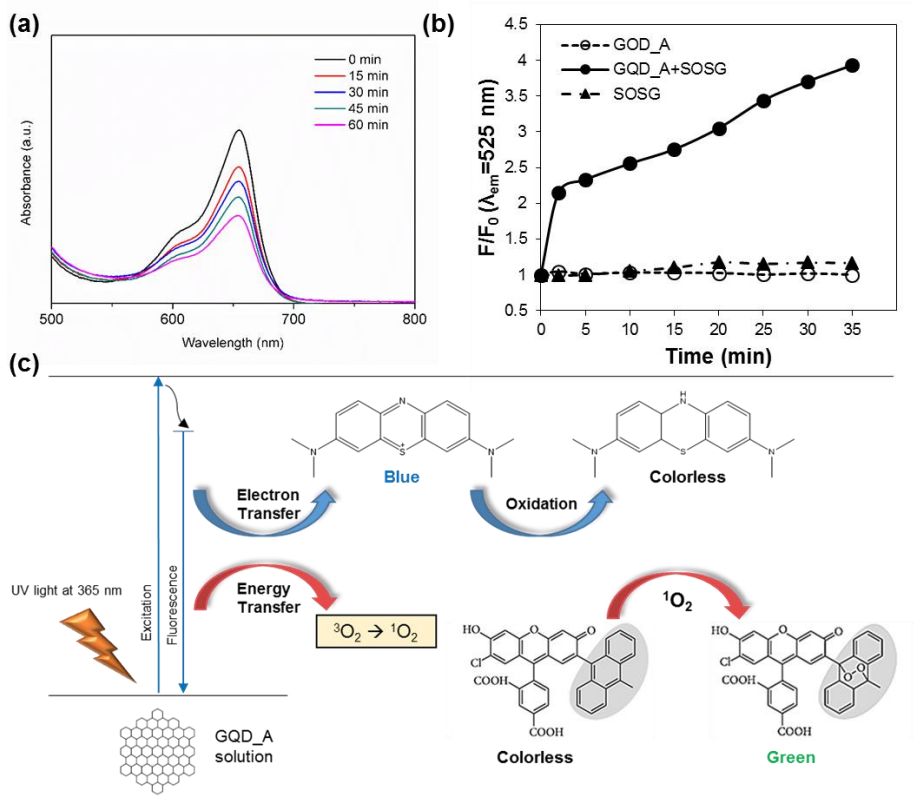

Figure 3. 24. Study of ROS generation. (a) Absorbance spectrum of 3 mL of GQDs_A and 10 μM of MB (in anhydrous ethanol) with UV irradiation related to Type Ⅰ ROS generation. (b) Singlet oxygen detection assay for after UV irradiation related to Type Ⅱ ROS generation. (c) Energy/electron transfer diagram.

We next investigated the photodynamic therapeutic efficacy of GQDs in HeLa cells. After 12 h of treatment with armchair GQDs and zigzag GQDs, the cells were irradiated with a 365 nm LED (50 mW/cm^2) for 10 sec, followed by conventional live/dead assay. As shown in Figure 3.25a, red fluorescence at 572 nm (λ_{ex}=547 nm) and green fluorescence at 520 nm (λ_{ex}=490 nm)

respectively originated from dead cells and live cells were clearly distinguished across the boundary line of irradiated and non-irradiated region in armchair GQDs treated cells whereas only green fluorescence was observed in zigzag GQDs treated cells. Next, we evaluated irradiation time-dependent and particle dose-dependent PDT effect *in vitro*. HeLa cells were treated with various concentration of armchair GQDs (0 ~ 20 μg/mL) and irradiated with various times (0 ~ 60 sec) by 365 nm LED (50 mW/cm^2), followed by CCK-8 cell viability assay. The IC_{50} value of armchair GQDs was revealed as about 20 μg/mL with light irradiation for 10 sec (Figure 3.25b and c), which showed low cytotoxicity itself without irradiation. Taken together, the results supported efficient PDT effect of armchair GQDs in live cells.

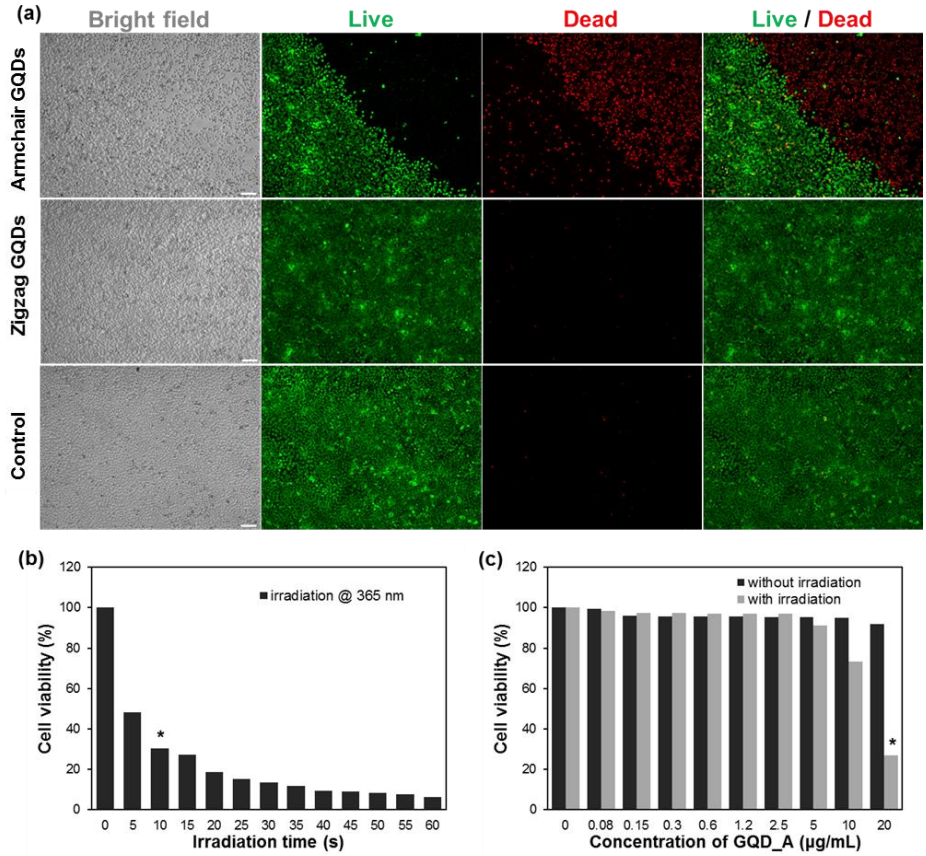

Figure 3. 25. (a) Fluorescence images of HeLa cells treated with GQDs (20 μg/mL) for 12 h followed by irradiation for 10 sec with 365 nm light (50 mW/cm^2). Live and dead cells colored green and red respectively after live/dead assay. Scale bar is 100 μm. (b,c) Viability of HeLa cells related to irradiation time and concentration of armchair GQD. (b) Cell viability of HeLa cells treated with armchair GQD (20 μg/mL) for 12 h followed by irradiation in various times with 365 nm light (50 mW/cm^2). (c) Cell viability of HeLa cells treated with armchair GQD (0 – 20 μg/mL) for 12 h followed by irradiation for 10 sec with 365 nm light (50 mW/cm^2).

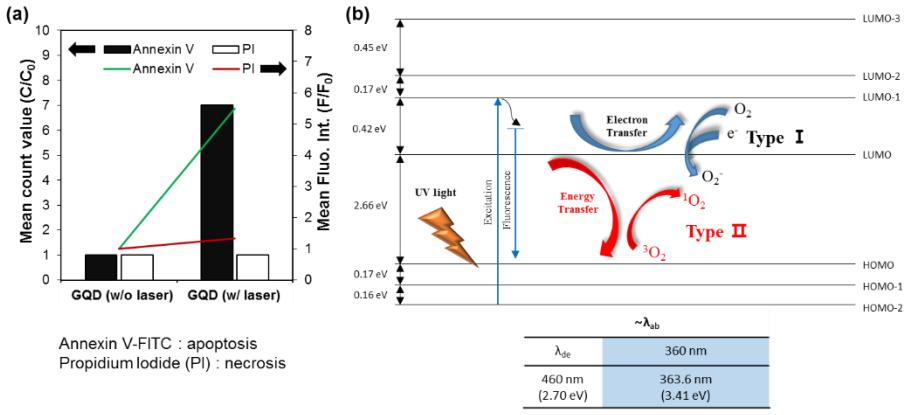

Figure 3. 26. (a) Mean cell population (bar graph, left) and fluorescence intensity (line graph, right) of HeLa cells treated with GQDs (20 μg/mL) for 12 h followed by irradiation for 10 sec with 365 nm light (50 mW/cm^2) represent apoptotic cells stained with annexin V-FITC and necrotic cells stained with propidium iodide (PI), respectively. (b) Energy level diagram of $^1O_2$ generation mechanisms by armchair GQD.

Based on the successful demonstration of PDT effect *in vitro*, we finally investigated the mechanism of armchair GQDs based photodynamic phenomenon. We first performed the quantification of apoptotic and necrotic cells through flow cytometry analysis by staining with Annexin V-FITC and propidium iodide (PI), respectively to figure out the cause of cell death by PDT of GQDs. Figure 3.26a showed that apoptotic cells were dominant in armchair GQDs treated cells and light irradiation compared to necrotic cells suggesting that GQDs based PDT was affected on intracellular apoptosis signal pathway.

Type Ⅱ and Ⅰ in PDT describes the energy diagram of armchair GQDs in Figure 3.26b. Kim et al. reported size-controllable fabrication of GQDs and their energy diagram.[41] However, energy level studies were performed by a mixed solution of armchair and zigzag GQDs. As results of our ongoing research efforts to investigate GQDs, Lee et al. showed the optical difference between zigzag and armchiar GQDs.[55] Based on the previous research, we research the PDT effect, depending on armchiar and zigzag GQDs. The cancer cells are only destroyed by armchair GQDs when irradiated light. It should mention that Type Ⅱ process in PDT involves the energy diagram of armchair GQDs. In previous report,[55] the PL peaks of armchair GQDs are observed at near 305, 360, 430, 400, 380, 335, and 465 nm. In the case of the solution, a mixture of zigzag and armchair GQDs, a peak of 290 nm was shown.[41] However, the peak can be a peak indicated by zigzag GQDs. The schematic of the electric structure of armchair GQDs can be re-established using PL and PLE measured data[55] (see Figure 3.18). In the PDT experiment, 365 ± 20 nm light was used. When armchair GQDs were irradiated with the light, the excited state electrons absorbed at 3.41 and 3.25 eV as shown in Figure 3.27 and 3.26b. Thus, electrons in HOMO-1 and HOMO-2 are excited to LUMO-1, then high energy electrons descend to be stable states. In here, the singlet oxygen is generated by this energy, involving Type Ⅱ process. Therefore, it can indirectly confirm Type Ⅱ

process of armchair GQDs. For the Type Ⅰ, Moreover, the generation of singlet oxygen (SO) was quantitatively probed by monitoring the intensified green fluorescence of singlet oxygen sensor green (SOSG) at 530 nm (λ_{ex}=504 nm) upon generation of SO. Figure 3.24b showed that SO was generated via light-induced armchair GQDs activation. Energy/electron transfer diagram of armchair GQDs for Type Ⅰ and Ⅱ is exhibited in Figure 3.24c.

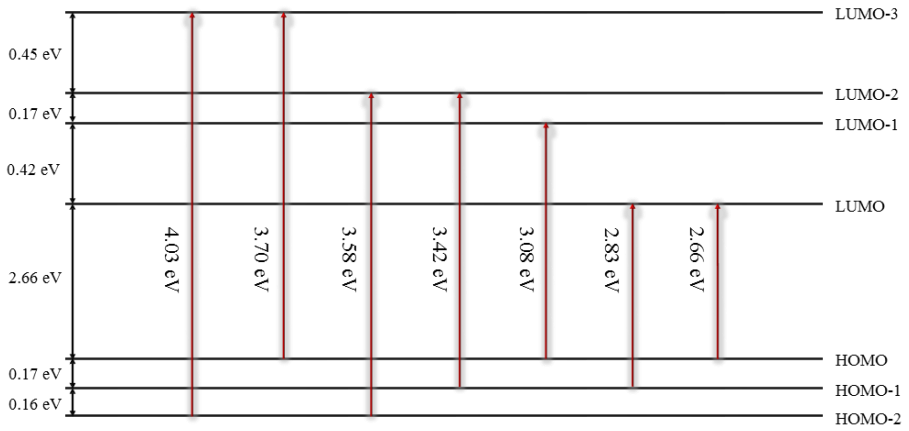

Figure 3. 27. Schematic of the electric structure of armchair GQDs.

On the basis of the IC_{50} values *in vitro*, we next investigated the biodistribution and photodynamic therapeutic efficacy *in vivo* using xenograft mouse model. Tumor-bearing mice were prepared by subcutaneously injecting a suspension of the HeLa cells (6×10^6 cells) in 100 μL of sterilized phosphate buffered saline (PBS, pH 7.4) into Balb/c male nude mice (5-week old).

To monitor the biodistribution of armchair GQDs, the fluorescence signals from the tumors were obtained after 24 h of intravenous injection of armchair GQDs and PBS as a control. As shown in Figure 3.28, the intense green fluorescence of armchair GQDs was observed in tumors treated with armchair GQDs but not in PBS-treated ones. We also found notable fluorescence signal in armchair GQDs treated tumor tissue sections dissected from the mice in comparison with other tumor groups (Figure 3.28b and 3.29). The green fluorescence corresponding to armchair GQDs was also visible in livers and kidney of armchair GQDs treated mouse, which could be explained by clearance of various nanoparticles through the reticuloendothelial system (RES) and renal clearance.

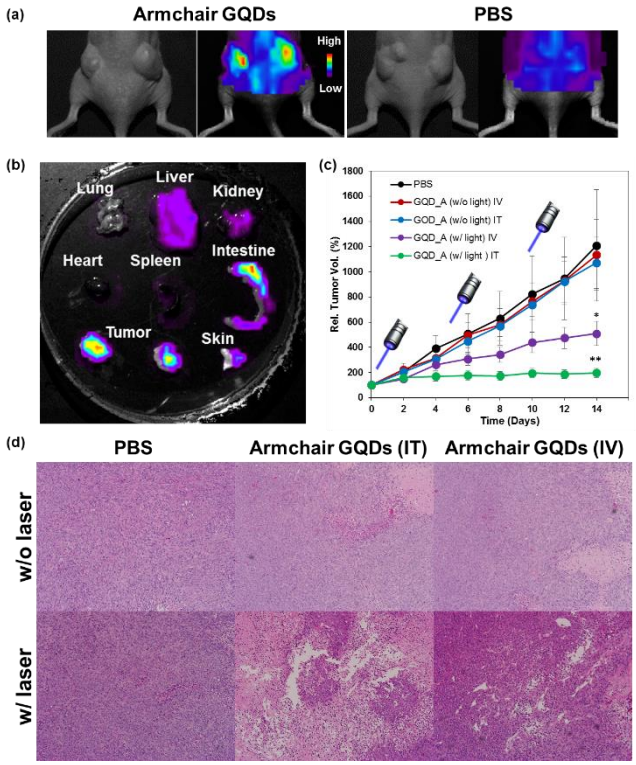

Figure 3. 28. (a) Bright field and fluorescence image of armchair GQDs (λ_{ex} = 470 nm) in tumor-bearing mice were obtained after 24 h of intravenous injection of GQD and PBS. (b) Ex vivo fluorescence images of major organs of GQD treated mice. The fluorescent signals corresponding to armchair GQDs (λ_{ex} = 470 nm) from major organs, tumor, and skin were obtained after 24 h of IV injection of GQD into tumor-bearing mice. (c) Relative tumor volumes measured over time after the tumor-bearing mice were treated with GQD and PBS. Irradiation was dosed using 365 nm LED at 50 mW/cm^2 for 20 s three times (0, 5, 10 days) and tumor volume was measured over 14 days. P values were calculated by Student' s t-test, * for $p<0.05$, ** for $p<0.01$, n=4. (IV: Intravenous injection, IT: Intratumoral injection).

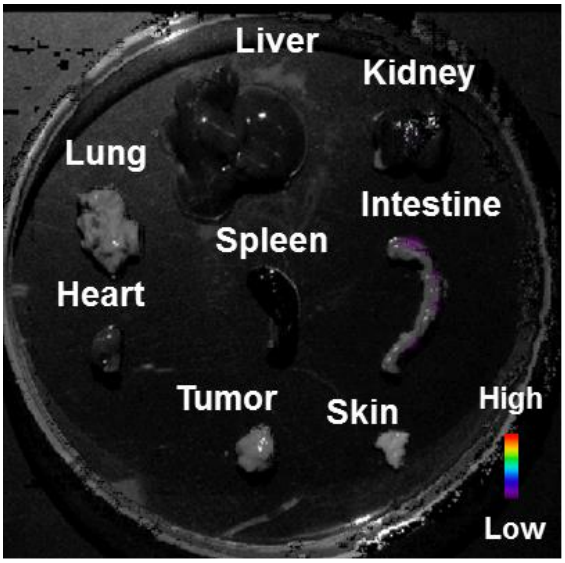

Figure 3. 29. Ex vivo fluorescence images of major organs of mice injected with PBS intravenously.

Finally, we investigated the photodynamic anti-tumor activity of armchair GQDs against human cancer xenograft. Each tumor was grown up to 50 mm^3 in volume and then treated with armchair GQDs (20 μg/mL), and PBS by intravenous and intratumoral injection. After 24 h of injection, the light was irradiated with 365 nm LED (50 mW/cm^2) for 10 sec, and the changes of tumor volume in each group were monitored for 2 weeks. As shown in Figure 3.28c, tumor growth in the mice treated with armchair GQDs and laser irradiation was significantly inhibited. However, those in other groups without laser irradiation showed no notable difference with tumor volume compared to control groups, supporting that armchair GQDs mediated PDT effectively induced cell death and inhibited the growth of tumors *in vivo*. Based on

the statistical significant difference from the tumors between armchair GQDs with laser-treated group and other groups, hematoxylin and eosin (H&E) staining of tumor sections was performed at 14 days post treatment. As shown in Figure 3.28d, remarkably intensive cancer apoptosis was observed only in tumors with armchair GQDs (with laser irradiation) treatment, which is a contrast to PBS-treated group and without laser irradiation groups. Moreover, the histological study with infiltrated and stained tumor section showed highly pleomorphic nuclei without the systemic toxicity of any certain toxicological necrosis in major organs (i.e., liver, heart) from the mice treated with armchair GQDs compared to PBS (Figure 3.29). This result reveals that our GQD based PDT is adaptable for *in vivo* systemic application with low cytotoxicity.

In conclusion, a number of scientists have studied PDT using GQDs, which are one of carbon nanomaterials. However, the photodynamic effects of GQDs was not precisely studied how GQDs destroy cancer cells. We investigated photodynamic effect by using the different edge structures of GQDs. By treating cancellous cells with armchair GQDs and irradiation with 365 nm light, these cells were killed, while for zigzag GQDs, they are by exposing not killed, which means that Type Ⅰ and Type Ⅱ phenomena occurred only in armchair GQDs, not in zigzag GQDs. As a result, it confirms that the photodynamic effect of GQDs is based on their edge structure.

Chapter 4

Fabrication of dispersible graphene flakes using thermal plasma jet and their thin films for solar cells

Low- and high-magnification SEM images of the raw carbon soot, without any treatment, produced by the injection of ethylene gas as a carbon source are presented in Figure 4.1. The carbon soot was very pure and consisted of small-sized graphene flakes. Each graphene flake was very thin and transparent (see Figures 4.1 and 4.2). When the injection rate of ethylene gas was 500 sccm, the production rate based on the amount of graphene flakes collected in the chamber was approximately 1.5 g/h. The carbon soot was well dispersed by sonication in organic solvents such as ethanol, cyclohexane, and DMF. The dispersed solutions were very stable for several months (see Figure 4.3). However, in water, a very small amount of graphene flakes was dispersed even by sonication.

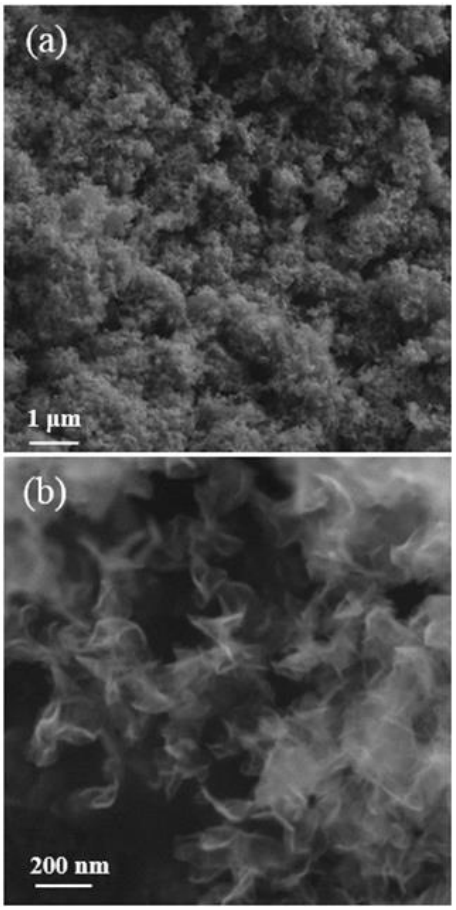

Figure 4. 1. Low- and high-magnification SEM images of graphene flakes.

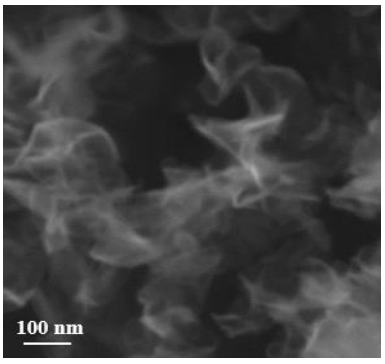

Figure 4. 2. The high-magnification SEM image of graphene flakes in Figure 4. 1b.

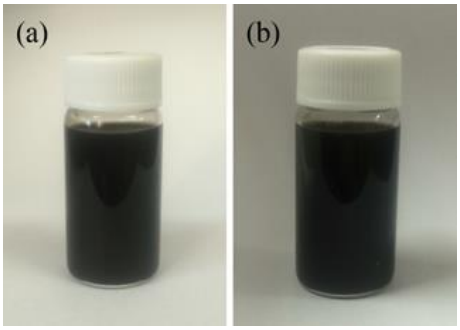

Figure 4. 3. Photographs of graphene dispersed in anhydrous ethanol: freshly prepared (a) and about 6 month old (b).

As mentioned in the introduction, when a low-density carbon atomic beam collides with the graphite plate (see Figure 2.3), graphene forms on the surface of the graphite plate by epitaxial growth and is then stripped away as graphene flakes by the collision force of Ar atoms, which compose the plasma gas. The injection rate of ethylene gas was critically affected by the production rate and purity of the carbon soot. The production rate of carbon soot decreased upon decreasing the injection rate of ethylene gas below 500 sccm. However, when the injection rate was somewhat higher than 500 sccm, in addition to graphene flakes, some impurities such as onion-type carbon materials were also produced. Upon increasing the injection rate of the carbon source, the density of carbon atoms of the carbon atomic beam increased. Therefore, during flow through the attached carbon tube, the collision probability between carbon atoms increased, and onion-type carbon materials[41,55], which are the dominant species in the fabrication of GQDs, could be formed by

the collision reactions. In the SEM and TEM images of carbon soot produced by injection of ethylene gas at 700 sccm, onion-type carbon materials are observed together with graphene flakes (see Figure 4.4).

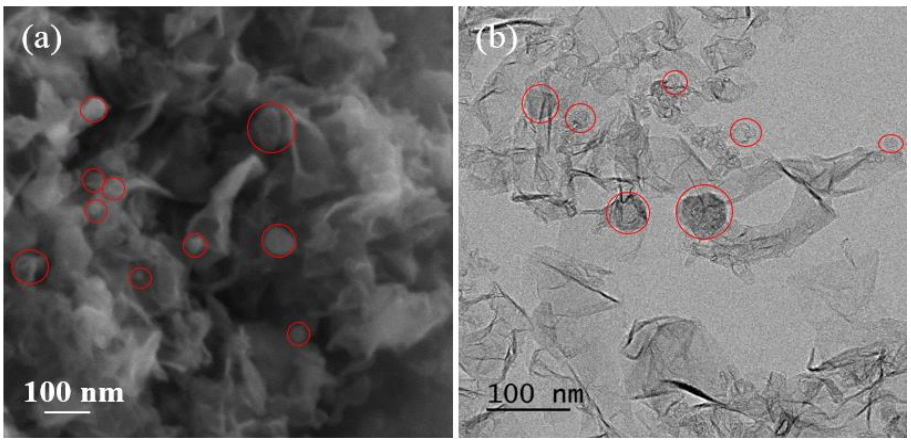

Figure 4. 4. (a) SEM and (b) TEM images of carbon soot produced by ethylene gas injection at 700 sccm into Ar plasma. Sphere shapes (marked as open circles) are onion type carbon materials.

Low- and high-magnification TEM images of the produced graphene are presented in Figure 4.5. The TEM sample was prepared by dropping graphene flake solution dispersed in ethanol on a TEM grid. In the low-magnification image, small-sized graphene flakes that are folded and overlap one other are observed, which made measuring the average size of graphene difficult. By our rough estimation, the average size was larger than 100 nm. In the high-resolution TEM image, fringes from the folded graphene are observed, where the number of fringes corresponds to the number of graphene layers.[103] Graphene

flakes were few layered. In Figures 4.5b and 4.6, three fringes can be observed along the edge. The carbon soot consisting of graphene flakes was well-dispersed by sonication in some solvents such as ethanol, cyclohexane, and DMF. The dispersibility of the graphene flakes attractive for several graphene flakes fabricated by the injection of ethanol are not dispersed in common solvents, which may be due to their relatively large average size (greater than 500 nm).[72] The dispersion property could be affected by oxygen inclusion during fabrication. However, in principle, oxygen is not contained in our fabrication because high purity ethylene and Ar gases are injected into the system as the carbon source and plasma gas, respectively. Indeed, according to the energy-dispersive X-ray spectroscopy (EDS) analysis, no oxygen was observed in our graphene flakes when they were not exposed to air (see Figures 4.7a and 4.8). This result indicates that our pristine graphene flakes contained no oxygen. However, when the graphene flakes were exposed to air, oxygen was included (see Figure 4.9). The XPS wide-scan spectrum and deconvoluted XPS C1s spectra are presented in Figures 4.7b and c, respectively. In the wide-scan spectrum, the C1s peak is very strong at 284.8 eV, and the O1s peak is very weak at 532 eV. In the deconvoluted spectra, the predominant peak at approximately 284.8 eV originates from sp^2 carbons, and the weak peak at 285.9 eV originates from sp^3 carbons.[104.105] The predominant peak reveals that the graphene

flakes consist of mostly sp^2 bonded carbons. The peaks derived from C-OH and O=C-OH are relatively weak at 286.5 and 288.5 eV, respectively. Although their intensities are very weak, the observation of these two peaks indicates that oxygen was present in the XPS sample. Because our pristine graphene flakes contained no oxygen, a very small percent of oxygen might be introduced in the preparation or loading process of the XPS sample. Actually, the graphene flakes were dispersed in ethanol by sonication under atmosphere, and the XPS sample was briefly exposed to air during loading into the XPS chamber.

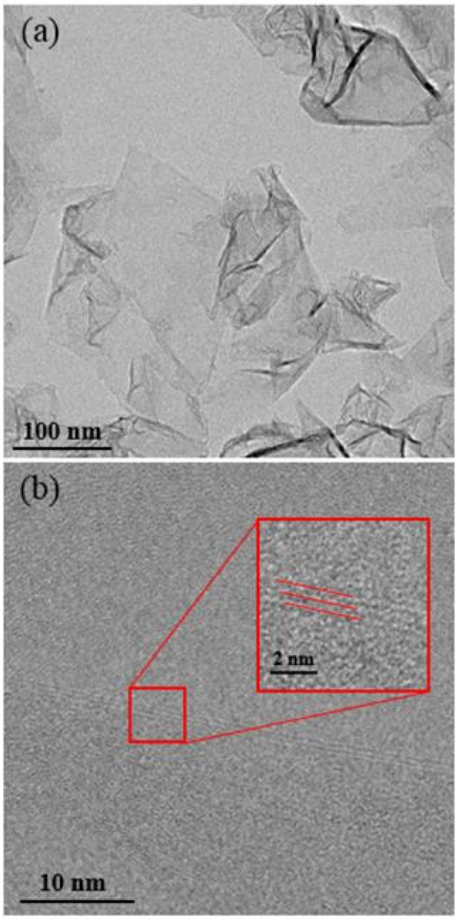

Figure 4. 5. Low- and high-magnification TEM images of

graphene flakes.

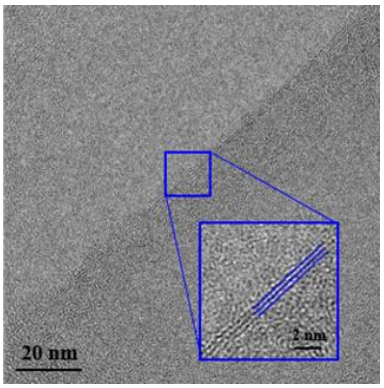

Figure 4. 6. The high-magnification TEM image of graphene flakes. Inset is straight lines to distinguish the fringes.

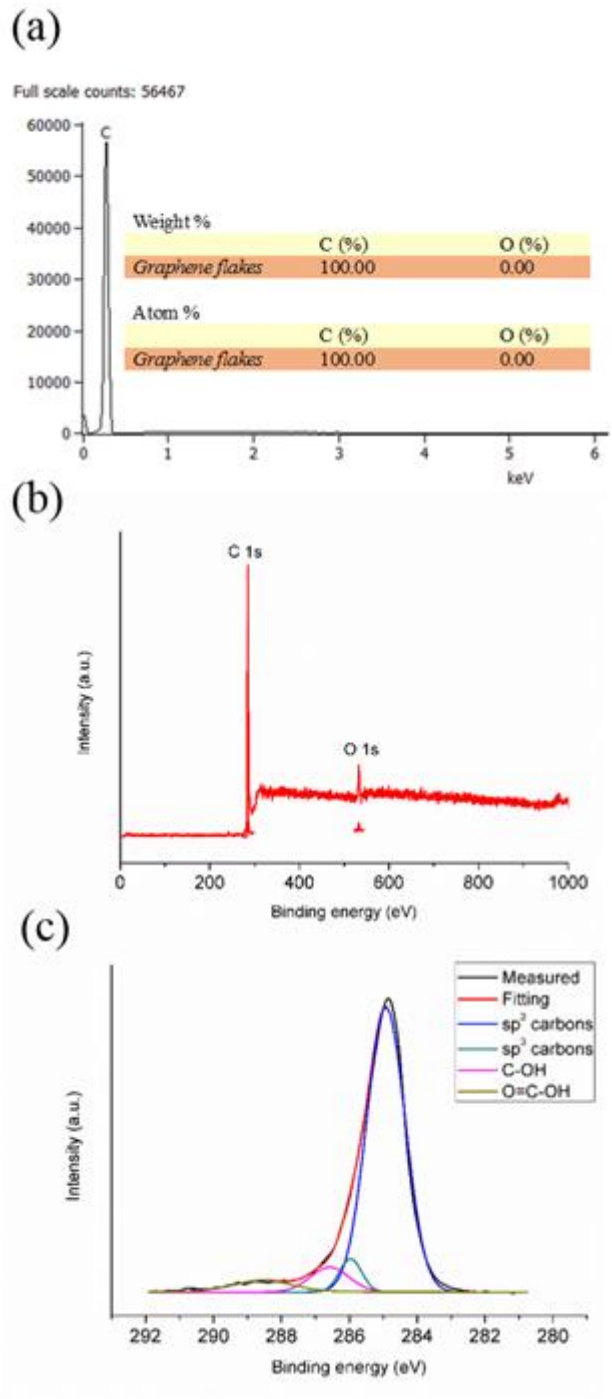

Figure 4. 7. (a) EDS spectrum and composition table, (b) XPS wide scan spectrum, and (C) C1s XPS spectra of graphene flakes.

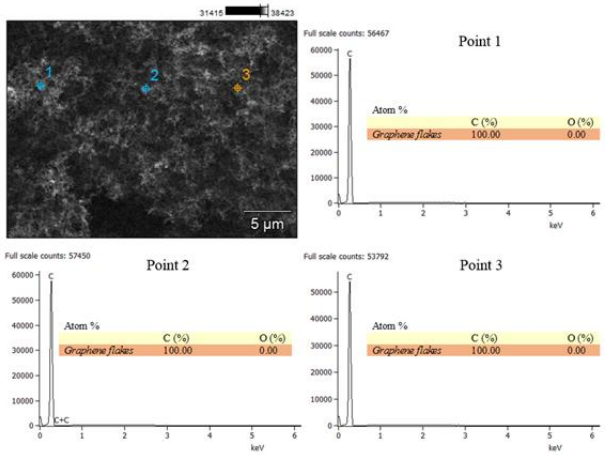

Figure 4. 8. The SEM image and EDS spectra of graphene flakes, not exposed to air. The average oxygen content of graphene flakes is zero. The spots marked as 1, 2, and 3 are the measured points.

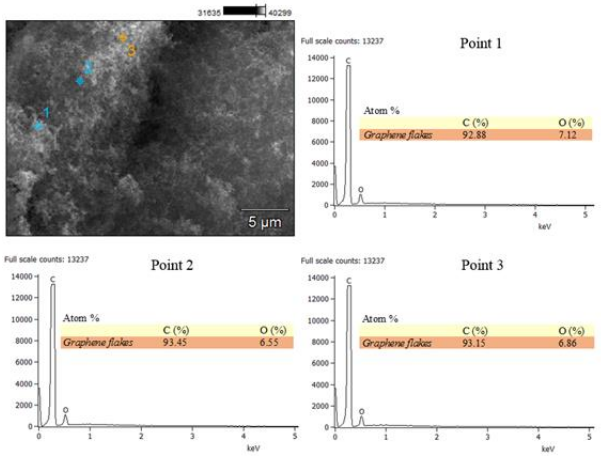

Figure 4. 9. The SEM image and EDS spectra of graphene flakes, exposed to air for 30 min. The The average oxygen content of graphene flakes is 6.84 atomic %. The spots marked as 1, 2, and 3 are the measured points.

The Raman spectra measured from a graphene flake film prepared by the electrophoretic method and from graphene flakes are presented in Figures 4.10a and b, respectively. The two spectra are almost the same. There are three typical graphene peaks; the D peak near 1360 cm^{-1}, G peak near 1594 cm^{-1}, and 2D peak near 2703 cm^{-1}. The G peak represents the E_{2g} vibrational mode, and the 2D band represents the second-order two-phonon mode. The D peak originates from the presence of structural disorders in graphene sheets.[106] The position and shape of the 2D peak has been used to distinguish single-layer, double-layer, and multi-layer graphene.[106-108] For single-layer graphene sheets, the peak is very sharp and appears at a Raman shift lower than 2700 cm^{-1}. Upon 514.5-nm excitation, the peak is located near 2700 cm^{-1} for double-layer sheets and near 2715 cm^{-1} for five-layer sheets.[106] Note that the Raman peak positions of graphene are altered by the excitation wavelength.[106] The position of the 2D peak is near 2703 cm^{-1}, which corresponds to the peak position of two- or three-layered graphene. This result agrees well with the TEM images (see Figure 4.5b). The D band is not Raman active for pristine graphene, such as highly oriented pyrolytic graphite (HOPG), but can be observed where symmetry is broken by edges or in samples with a high density of defects.[107] Therefore, the G/D intensity ratio can be used to determine the crystallinity of graphene with a higher ratio indicating better graphene

crystallinity. In the spectrum, the intensity of the G peak is relatively strong but not predominantly strong compared with that of the D peak. However, the edges of graphene sheets are always seen as defects. The size of our graphene is approximately 100 nm, and the ratio of edges is relatively large compared with that of large-sized graphene. Therefore, the G/D intensity ratio does not simply represent the crystallinity of our graphene flakes. Nevertheless, the predominantly strong peak derived from sp^2 carbons in the XPS spectrum may indicate that our graphene flakes exhibit good crystallinity.

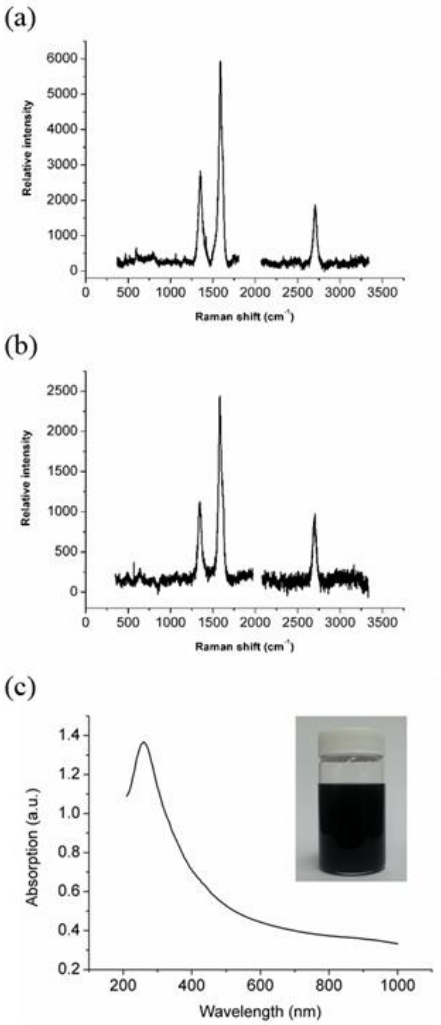

Figure 4. 10. Raman spectra measured from (a) a graphene flake film prepared by the electrophoretic method and (b) graphene flakes. (c) UV-vis absorption spectrum of graphene flakes dispersed in ethanol. The inset presents a photograph of a dispersed solution.

The graphene suspension exhibits a strong absorption in the UV region with a tail extending into the visible range (see Figure 4.10c). However, no photoluminescence (PL) was observed in

the visible region. We can consider at least two possible causes for the absence of PL. One possible cause is that the size of the graphene flakes (greater than 100 nm) is too large to have a band gap corresponding to visible light by quantum confinement.[1] The other possible cause is that the flakes may have neither carbene nor carbyne edge structures. GQDs produced using thermal plasma jet exhibit well-characterized PL depending on their edge structures.[55] Three types of GQDs have been identified by their edge structures: armchair GQDs with only carbyne edges, zigzag GQDs with only carbene edges, and hybrid GQDs with both carbyne and carbene edges in each dot.[40,99,100] The PL and PL excitation spectra of the hybrid GQDs respond to the combination of the spectra of zigzag and armchair GQDs. No characterized PL may indicate that their edges exhibit neither the carbene nor carbyne structure. As mentioned in the introduction, the GQDs are formed by the gas-phase collision reaction during flow through the carbon tube attached to the anode, whereas graphene flakes are produced by epitaxial growth on the graphite plate, which was placed 10 cm away from the end of the attached carbon tube. The two growth mechanisms are completely different from each other. In addition, their reaction temperatures might be very different. The plasma temperature is very high (approximately 10^4 K) and decreases upon increasing the distance from the plasma generation zone, which is located in the small gap between the cathode and anode.[72] Moreover, the graphite plate was not physically attached to the anode, and the temperature at the graphite plate might be much

lower than that at the inside of the carbon tube attached directly to the anode. When an ethylene molecule is atomized, two carbon and four hydrogen atoms are generated. Therefore, hydrogen atoms could be included in the structure of graphene. However, there is no hydrogen atom in the structures of carbene and carbyne. Carbene edges have two unshared valence electrons at each edge carbon atom, whereas carbyne edges have carbon triple bonds between two edge carbon atoms. GQDs are formed at a relatively high temperature, and no hydrogen atom could be included in their edge structures. However, graphene flakes are formed at a relatively low temperature. Therefore, hydrogen atoms could be included in the edge structures of graphene flakes. In fact, peaks corresponding to -CH_2- and -CH_3 were identified in the NMR spectrum (see Figure 4.11).

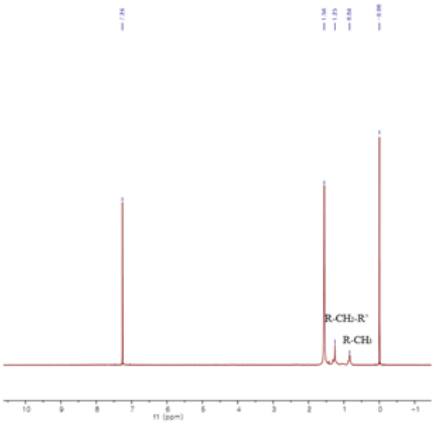

Figure 4. 11. ^{1}H–NMR NMR spectrum (500 MHz, $CDCl_3$) of graphene flakes at room temperature. The peaks at 1.25 and 0.84 ppm are due to $R-CH_2-R'$ and $R-CH_3$ protons of graphene flakes, respectively. The peak at 7.26 ppm is due to chloroform

($CDCl_3$), which is not deuterated, in $CDCl_3$. The peak at 1.56 ppm is due to water contained in $CDCl_3$ solvent as an impurity.

Low- and high-magnification SEM images of graphene flake films prepared using electrophoretic deposition (a, b), spray-coating (c, d), and interfacial assembling followed transferring (e, f) are presented in Figure 4.12. In the electrophoretic deposition, aluminum and graphite plates were used as the working and counter electrodes, respectively. Graphene flakes were deposited on an aluminum plate by applying a negative voltage, which indicates that the dispersed graphene flakes had a net positive charge. Although flakes were deposited flatly and finely, they were not deposited uniformly on a large area. Large-area films could be formed using spray-coating and interfacial assembling and transferring. Spray-coating is an easy process to manufacture thin films using a well-dispersible graphene suspension. However, relatively thick films were formed, and the surface was relatively rough, as observed in Figures 4.12c and d. Using the reported interfacial assembling followed transferring method,[97] a large graphene flake thin film was prepared on the liquid surface using a well-dispersed graphene flake suspension. When a volatile solvent such as EA was added to the mixture of water and graphene flake suspension in DMF, graphene flakes migrated toward the liquid surface via convective flow caused by the Rayleigh-Taylor instability[109]. The migrating graphene flakes

were fixed as a layer at the liquid surface through physical binding of their edge, which is known as Marangoni forces[110,111] (see Figure 2.4). The film could be easily transferred onto various substrates such as FTO glass and aluminum plate. The transferred film on FTO glass was relatively thin and uniform over a large area (see Figures 4.12e and f). The graphene film transferred on FTO glass was used as a counter electrode for DSSCs. It should be mentioned that the microstructures of our films are something like the reported graphene walls, which were directly grown on dielectric substrates by plasma enhanced chemical vapor deposition (PECVD) at 900 ° C.[112] The film of graphene walls was also used as a counter electrode for DSSCs. However, the energy conversion efficiency was relatively very low as 2.19%. Also, due to a relatively high fabrication temperature, it is very hard to use FTO glass as a substrate.

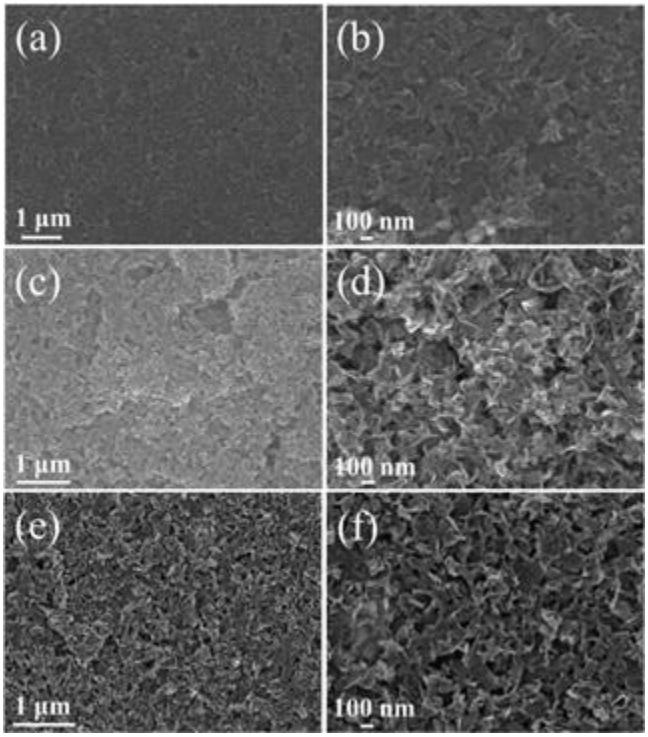

Figure 4. 12. Low- and high-magnification SEM images of graphene flakes deposited on (a, b) an Al plate by electrophoretic deposition, (c, d) FTO glass by spray-coating, and (e, f) FTO glass by interfacial assembling followed transferring.

The J-V curves measured in air mass 1.5 sunlight from the DSSCs based on TiO_2 nanoparticles (NPs) and N719 dye by employing graphene/FTO and conventional Pt/FTO electrodes as counter electrodes are presented in Figure 4.13. The graphene/FTO electrode was prepared by deposition of graphene flakes on FTO glass using the interfacial assembling followed transferring method. The photovoltaic parameters are listed in Table 4.1. For the DSSC with Pt/FTO electrode, the short-circuit current density (J_{sc}), open-circuit voltage (V_{oc}), fill factor

(FF), and power conversion efficiency (η) were 16.68 mA/cm^2, 0.78 V, 0.70%, and 9.07%, respectively. Here, we used the Pt/FTO electrode as the reference because Pt is a widely used cathode material owing to its high electrocatalytic activity toward the reduction of triiodide. It is generally believed that nanostructured platinum such as NPs improves the photoelectron conversion efficiency of DSSCs by providing a large surface area for triiodide reduction. For the DSSC with graphene/FTO electrode, J_{sc}, V_{oc}, FF, and η were 16.25 mA/cm^2, 0.78 V, 0.71%, and 9.03%, respectively. η was almost the same as that of the DSSC employing the Pt/FTO electrode (9.07%). However, in numerous reported works, DSSCs with graphene/FTO electrodes have exhibited a relatively lower efficiency than those with a Pt/FTO electrode.[113–116] In addition, the IPCE spectrum measured from the DSSC with a graphene flake/FTO electrode in the wavelength range of 400-700 nm is similar to that of the DSSC with the Pt/FTO electrode (see Figure 4.14).

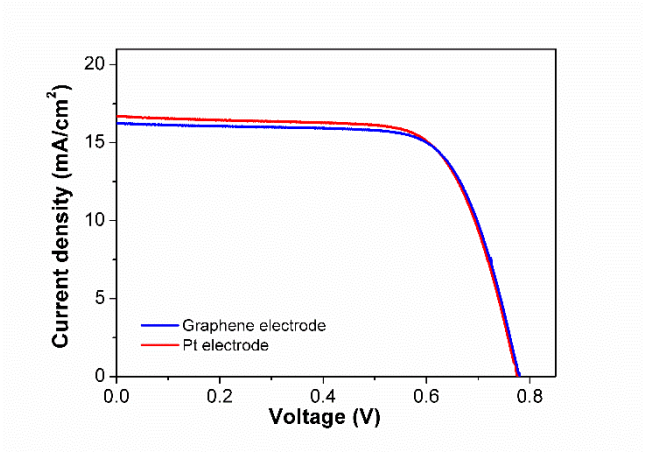

Figure 4. 13. J-V curves of the DSSCs based on TiO_2 NPs and N719 dye with Pt/FTO (red) and graphene/FTO (blue) electrodes.

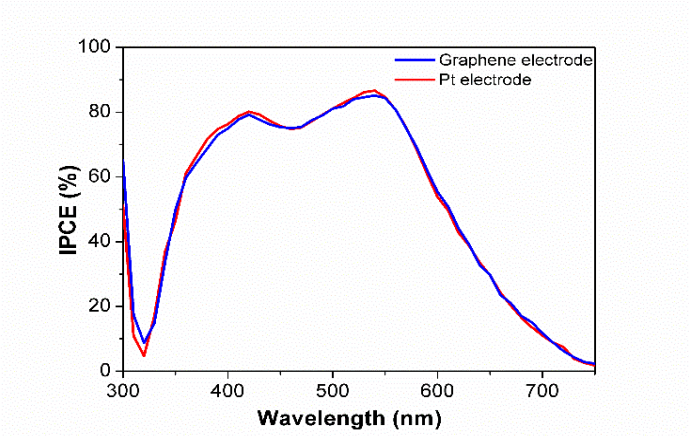

Figure 4. 14. IPCE spectra measured from the DSSCs with (red) Pt/FTO and (blue) graphene/FTO electrodes.

Table 4. 1. Photovoltaic properties of the DSSCs based on TiO_2 NPs and N719 dye with Pt/FTO and graphene/FTO electrodes.

Counter electrode	V_{oc} (v)	J_{sc} (mA/cm^2)	FF	η (%)
Pt/FTO electrode (reference)	0.78	16.68	0.70	9.07
Graphene/FTO electrode	0.78	16.25	0.71	9.03

CV curves measured from the graphene flakes/FTO and conventional Pt/FTO electrodes are presented in Figure 4.15. There are two typical pairs of oxidation-reduction peaks originating from $I_3^- + 2e^- \leftrightarrow 3I^-$ (i_{ox}/i_{red}) and $3I_2 + 2e^- \leftrightarrow 2I_3^-$ (ii_{ox}/ii_{red}) reactions. The former pair is related to the oxidation and reduction of I^-/I_3^- (i_{ox}/i_{red}), whereas the latter pair is related to the oxidation and reduction of I_2/I_3^- (ii_{ox}/ii_{red}). The redox potential of the former pair (i_{ox}/i_{red}) is important in this study because the reduction of I_3^- to I^- occurs on the counter electrode of DSSCs. The peak current intensity of i_{red} and peak-to-peak separation (E_{pp}) between i_{ox} and i_{red} are important parameters for characterizing the catalytic activities of the counter electrode. The high absolute intensity of i_{red} indicates a faster reduction velocity, which demonstrates the better ability of the counter electrode to reduce the I_3^- species to I^-.[117] The peak current intensity (i_{red}) of the graphene flake/FTO electrode was −1.09 mA, which is slightly higher in absolute value than that of the Pt/FTO electrode (−0.96 mA). This finding indicates that the graphene flake/FTO electrode exhibited a slightly higher catalytic rate for I^- regeneration than the Pt/FTO electrode. E_{pp} was 0.54 V for the graphene flake/FTO electrode and 0.55 V for the Pt/FTO electrode. The value of E_{pp} is known to be inversely proportional to the charge transfer rate,[118] which indicates that with decreasing E_{pp}, the catalytic activity is improved. Therefore, it is concluded that the graphene flake/FTO electrode exhibited

a slightly better catalytic activity than the Pt/FTO electrode. Based on the efficiency, IPCE, and CV results, it is concluded that the graphene flake/FTO and Pt/FTO electrodes exhibit similar abilities as counter electrodes for DSSCs. Therefore, our graphene flake/FTO electrode could be used as a substitute for the conventional Pt/FTO counter electrode for DSSCs as graphene flakes are much less expensive than Pt.

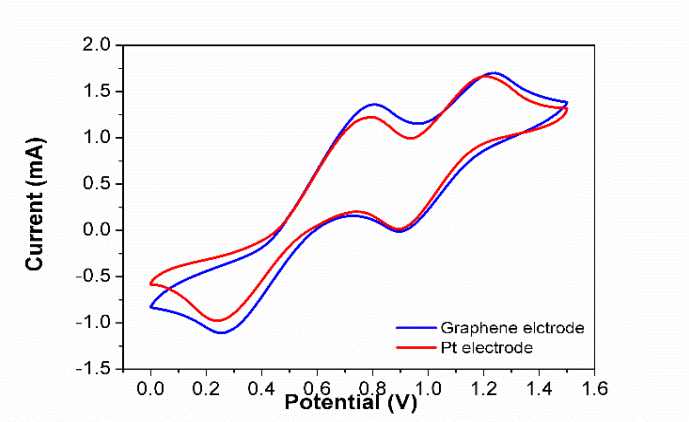

Figure 4. 15. CV curves measured from (red) Pt/FTO and (blue) graphene/FTO electrodes.

In the fabrication of graphene flakes, we attached a relatively long carbon tube (20 cm in length) to the anode and placed a graphite plate 10 cm away from the end of the carbon tube (see Figure 2.3). The attached carbon tube and graphite plate perform critical roles. The graphene flakes were prepared by epitaxial growth when a carbon atomic beam with appropriate energy collided with the graphite plate. No graphene was formed when a

silicon plate was used instead of a graphite plate. The attached carbon tube may perform at least two important roles: the carbon atomic beam generated is reduced significantly in its kinetic energy during flow through a relatively long carbon tube and also becomes homogeneous by collision between carbon atoms or by collision of carbon atoms with the inner surface of the carbon tube. The crystalline structure of the fabricated graphene may be affected by the homogeneity of the carbon atomic beam. The carbon atomic beam is dispersed after passing the end of the attached carbon tube. Therefore, the kinetic energy of the beam might be greatly reduced when moving from the end of the tube to the graphite plate, which was placed 10 cm away from the end of the tube. In addition, the gap between the graphite plate and end of the attached carbon tube affects the number of carbon atoms with the surface and surface It is clear that the number of carbon atoms with the surface and surface he injection rate of Ar plasma gas was 16.0 L/min and that of ethylene was 0.5 L/min (500 sccm).

In conclusions, we have succeeded in fabricating dispersible graphene flakes in common solvents using a thermal plasma jet system. The pristine graphene flakes produced by the injection of ethylene gas (500 sccm) were very pure, contained no oxygen, and were few layered. Although their average size was larger than 100 nm, they were well-dispersed in common organic solvents by sonication. The production rate of graphene flakes

based on the collected amount was approximately 1.5 g/h. Because of their good dispersibility in solvents, thin films of the graphene flakes could be fabricated using electrophoretic deposition, spray-coating, and interfacial assembling and transferring. We have demonstrated that the thin films could be used as a counter electrode for DSSCs. The electrocatalytic activity of the graphene flakes toward the reduction of triiodide was similar to that of Pt NPs. In addition to this specific application, dispersible graphene could be used in the fabrication of composites as well as various energy storage, sensor, and electronic devices.

Chapter 5

Fabrication of onion-type carbon using thermal plasma jet and their photothermal effects

In this study, we have confirmed a possibility to the field of biomedicine by onion-type carbon, which was prepared by using thermal plasma jet. A schematic of fabrication and application using onion-type carbon is presented in Figure 1.4. When Ar plasma is formed, ethylene gas is injected to carbon tube. The carbon bond between carbon atoms of ethylene is broken by the strong energy of the plasma, and then a carbon atom beam is formed. A gas collision reaction was generated in the attached carbon tube by the carbon atom beam (See Figure 1.4). The produced carbon soot includes about 10% of GQDs. The GQDs show emission of luminescence when irradiating light of specific wavelength. Carbon soots, thus, are washed by ethanol to remove GQDs. Carbon soots are clearly washed, and GQDs are washed away with ethanol. After that, when exposing the specific light on carbon soot, onion-type carbon have no photoluminescence. Using this pure onion carbon, we investigated properties of onion-type carbon such as photothermal effect and cytotoxicity into cells.

The production rate of onion-type carbon is 36 g per hour, which can be mass-produced when the thermal plasma jet is enlarged, as shown in Figure 5.1. The dispersibility of carbon nanomaterials is a very important factor in applications of various fields. Generally, graphene and carbon nanotube are widely used between carbon nanoamterials. However, there is a limit to applications that are not superior in dispersibility. Thus, we need

dispersible carbon nanomaterials. The excellent dispersibilty of onion-type carbon can be used to achieve purposes of applications in various fields including biomedicine.

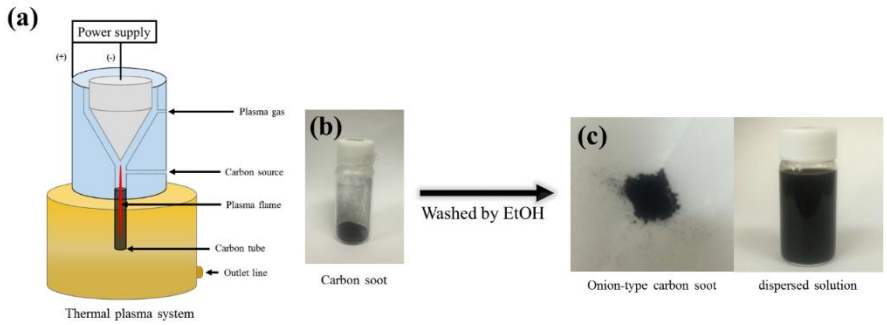

Figure 5. 1. Thermal plasma system, (b) the produced carbon soot, (c) onion-type carbon and dispersed solution.

The TEM sample was prepared by droping the dispersed onion-type carbon in ethanol on the TEM grid. The onion-type carbon in the low-magnification image of Figure 5.2a exhibited a very similar size of dots and stucked to each other. The average size of onion-type carbon is from 15 nanometers to 20 nanometers in the TEM image. In high-magnification TEM image of Figure 5.2b, the cross-sectional shape after cutting an onion is seen. It is clear that this material is onion-type carbon because of the fact that the material was produced by Ar gas and the carbon source only.

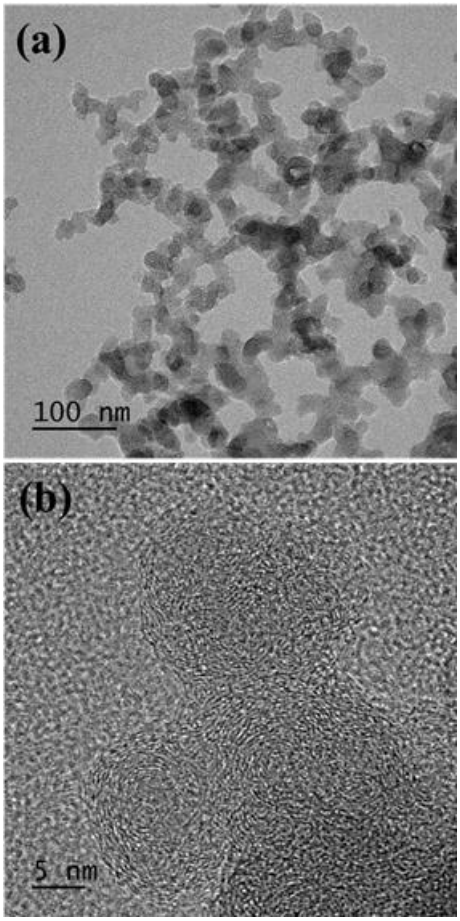

Figure 5. 2. Low- and high-magnification TEM images of onion-type carbon.

The prepared onion-type carbon has good dispersibility in common solvent. The onion-type carbon is placed into ethanol, and dispersible onion-type carbon solution is prepared after 15 minutes in bath sonication (see Figure 5.1c). The solution was analyzed by UV/vis spectroscopy. In Figure 5.3a, the onion-type carbon solution absorbed all light from UV to NIR regions. The absorption region of onion-type carbon can be assumed that it is superior light absorption than that of graphane. The first reason

is that graphene is mostly fabricated using large black carbon with other chemical reactions. Thus, defects and oxygen species between carbon atoms of graphene can be formed during synthesis, which mean a damage of the carbon double bonds in graphene. These defect and oxygen prevent electron migration and reduce the absorption of the NIR region. The second reason is that graphene has not been a good dispersibility. It is known that various functional groups of graphene should be synthesized in order to improve better dispersibility in solvents. Therefore, onion-type carbon has superior dispersibility and better light absorption than graphene in the same concentration.

In Figure 5.3b, onion-type carbon solution was irradiated with light of 808 nm, and concentration of the solution was 0.1 mg/ml in anhydrous ethanol. The temperature of onion-type carbon solution was increased, while the temperature of pure ethanol was not increased when irradiating NIR light. It is generally known that cancer cells are generally destroyed at around 40 °C. In Figure 4b, temperature of the solution was already at over 40 °C after 120s, and temperature of the solution was at over 45 °C after 150s, then rising rate of temperature was gradually lowered. In the analysis of the temperature change of the solution, it showed enough temperture to destroy the cancer cell when irradiated with NIR light. It was also expected that heat would be generated more by the increase of concentration although the solution of the concentration in this analysis was only 0.1 mg/ml.

As a result, it demonstrates that onion-type carbon has a photothermal effect.

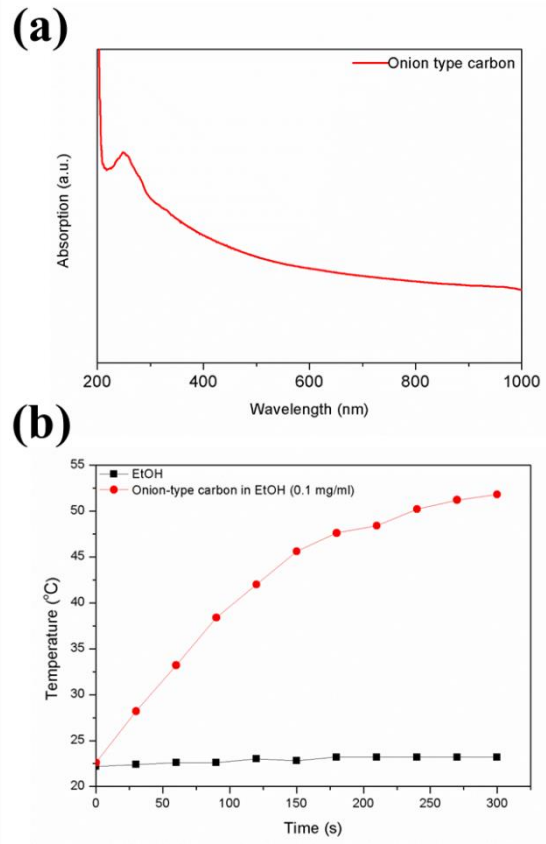

Figure 5. 3. (a) UV/vis absorption spectrum of onion-type carbon dispersed in ethanol (b) the change of temperatures of onion-type carbon solution showed that the temperature rose with the period of NIR irradiation (0 - 300s).

It is essential to confirm cytotoxicity in order to use materials, having photothermal effect, in biomedical science. It was treated to Human cervical carcinoma (HeLa) cells as a model to

investigate the cytotoxicity of onion-type carbon. Figure 5.4a presents that more than 98% of the HeLa cells remained even when the concentration of onion-type carbon was 0.5 mg / ml. It seems that the toxicity of onion-type carbon is very low.

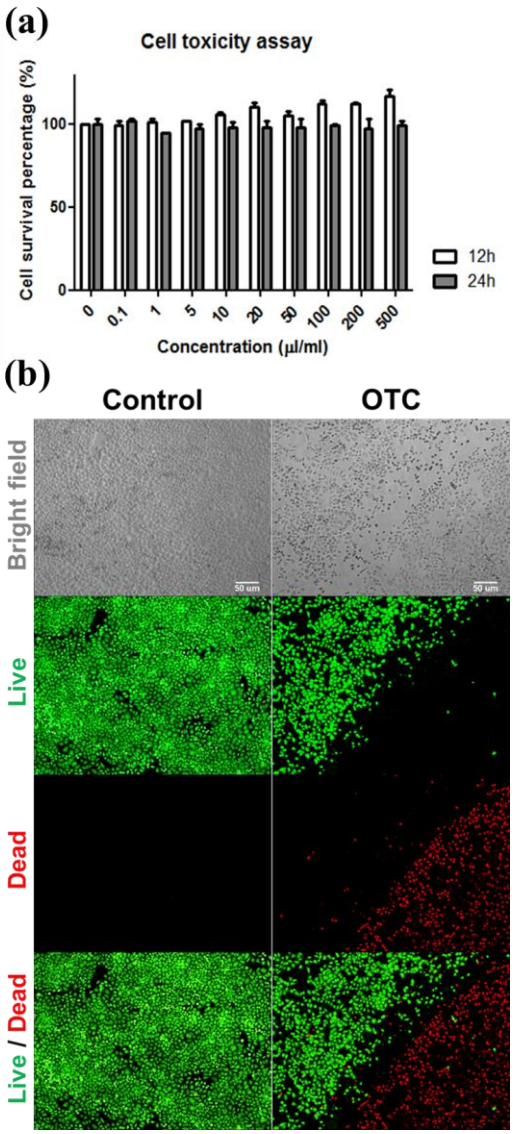

Figure 5. 4. (a) Cell viability of HeLa cells treated with onion-type carbon (0 – 500 μg/mL) for 12 and 24 h. (b) Bright field

and fluorescence microscope image from HeLa cells treated with onion-type carbon (OTC, 50 μg/mL) after laser irradiation (808 nm, 2 W/cm^2 for 10 min). Green fluorescence from living cells stained with Calcein AM at 520 nm (λ_{ex}=490) and red fluorescence from dead cells stained with Ethidium homodimer-1 at 572 nm (λ_{ex}=541) were obtained. Photothermal effect induced cell death appeared in onion-type carbon treated cells only. Scale bar is 50 μm.

Finally, we investigated the photothermal therapeutic efficacy of onion-type carbon in HeLa cells, which is a human cervical cancer cell. After confirming that the treatment of onion-type carbon (upto ~500 μg/mL) to HeLa cells shows more than 98% viability (Figure 5.4a), we evaluated the cell death *via* photothemal effect. The cells treated with onion-type carbon (50 μg/mL) were irradiated with an 808 nm laser (2 W/cm^2) for 10 min, followed by a conventional live/dead assay. As shown in Figure 5.4b, the green fluorescence at 520 nm (λ_{ex}=490 nm) and red fluorescence at 572 nm (λ_{ex}=541 nm) respectively resulted from live cells and dead cells were clearly distinct across the boundary of non-irradiated and irradiated region in the onion-type carbon treated cells whereas only green fluorescence was observed in the control group. Taken together, the results demonstrated efficient photothermal therapy of the onion-type carbon in live cells with low cytotoxicity of onion-

type carbon itself.

In conclusion, we have produced onion-type carbon as a new method using thermal plasma jet. Onion-type carbon was a promising carbon nanomaterial before discovery of graphene and carbon nanotubes. However, various studies of onion-type carbon were limited due to high-cost manufacture. The method for onion-type carbon using thermal plasma jet can be easily fabricated relatively and low-cost. In addition, onion-type carbon was produced by using only Ar and a carbon source. We confirmed the possibility of application to biomedicine using onion-type carbon. The onion-type carbon solution absorbs all light including NIR region and has excellent dispersibility. We proved that heat was generated in onion-type carbon solution when irradiating light of the infrared region, and very low toxicity was invested when HeLa cells were treated with onion-type carbon. It is proved that onion-type carbon has a photothermal effect and represents a new possibility to destroy cancer cells.

References

[1] Ponomarenko LA, Schedin F, Katsnelson MI, Yang R, Hill EW, Novoselov KS, et al. Chaotic dirac billiard in graphene quantum dots. *Science* 2008;320:356-8.

[2] Novoselov KS, Geim AK, Morozov SV, Jiang D, Zhang Y, Dubonos SV, et al. Electric field effect in atomically thin carbon films. *Science* 2004;306:666-9.

[3] Yan X, Cui X, Li B, Li L. Large, solution-processable graphene quantum dots as light absorbers for photovoltaics. *Nano Lett* 2010;10:1869-73.

[4] Neubeck S, Ponomarenko LA, Freitag F, Giesbers AJM, Zeitler U, Morozov SV, et al. From one electron to one hole: Quasiparticle counting in graphene quantum dots determined by electrochemical and plasma etching. *Small* 2010;6:1469-73.

[5] Li L, Yan X. Colloidal graphene quantum dots. *J Phys Chem Lett* 2010;1:2572-6.

[6] Li M, Wu W, Ren W, Cheng H, Tang N, Zhong W, et al. Synthesis and upconversion luminescence of N-doped graphene quantum dots. *Appl Phys Lett* 2012;101:103107.

[7] Kim S, Hwang SW, Kim M-K, Shin DY, Shin DH, Kim CO, et al. Anomalous behaviors of visible luminescence from graphene quantum dots: Interplay between size and shape. *ACS Nano* 2012;6:8203-8.

[8] Mueller ML, Yan X, McGuire JA, Li L. Triplet states and electronic relaxation in photoexcited graphene quantum dots. *Nano Lett* 2010;10:2679-82.

[9] Ritter KA, Lyding JW. The influence of edge structure on the electronic properties of graphene quantum dots and nanoribbons. *Nat Mater* 2009;8:235-42.

[10] Peng J, Gao W, Gupta BK, Liu Z, Ge L, Song L, et al. Graphene quantum dots derived from carbon fibers. *Nano Lett* 2012;12:844-9.

[11] Cheng H, Zhao Y, Fan Y, Xie X, Qu L, Shi G. Graphene-quantum-dot assembled nanotubes: A new platform for efficient raman enhancement. *ACS Nano* 2012;6:2237-44.

[12] Zhu S, Zhang J, Qiao C, Tang S, Li Y, Yuan W, et al. Strongly green-photoluminescent graphene quantum dots for bioimaging applications. *Chem Commun* 2011;47:6858-60.

[13] Jing Y, Zhu Y, Yang X, Shen J, Li C. Ultrasound-triggered smart drug release from multifunctional core-shell capsules one-step fabricated by coaxial electrospray method. *Langmuir* 2010;27:1175-80.

[14] Sun X, Liu Z, Welsher K, Robinson J, Goodwin A, Zaric S, et al. Nano-graphene oxide for cellular imaging and drug delivery. *Nano Lett* 2008;1:203-12.

[15] Gupta V, Chaudhary N, Srivastava R, Sharma GD, Bhardwaj R, Chand S. Luminscent graphene quantum dots for organic photovoltaic devices. *J Am Chem Soc* 2011;133:9960-3.

[16] Prezzi D, Varsano D, Ruini A, Marini A, Molinari E. Optical properties of graphene nanoribbons: The role of many-body effects. *Phys Rev B* 2008;77:041404.

[17] Yang L, Cohen ML, Louie SG. Excitonic effects in the optical

spectra of graphene nanoribbons. *Nano Lett* 2007;7:3112–5.

[18] Yang L, Cohen ML, Louie SG. Magnetic edge–state excitons in zigzag graphene nanoribbons. *Phys Rev Lett* 2008;101:186401.

[19] Zhu X, Su H. Excitons of edge and surface functionalized graphene nanoribbons. *J Phys Chem C* 2010;114:17257–62.

[20] Hsu H, Reichl LE. Selection rule for the optical absorption of graphene nanoribbons. *Phys Rev B* 2007;76:045418.

[21] Goerbig MO, Fuchs JN, Kechedzhi K, Fal' ko VI. Filling–factor–dependent magnetophonon resonance in graphene. *Phys Rev Lett* 2007;99:087402.

[22] Gusynin VP, Sharapov SG, Carbotte JP. Anomalous absorption line in the magneto–optical response of graphene. *Phys Rev Lett* 2007;98:157402.

[23] Ozyilmaz B, Jarillo–Herrero P, Efetov D, Abanin DA, Levitov LS, Kim P. Electronic transport and quantum hall effect in bipolar graphene p–n–p junctions. *Phys Rev Lett* 2007;99:166804.

[24] Pan DY, Zhang JC, Li Z, Wu MH. Hydrothermal route for cutting graphene sheets into blue–luminescent graphene quantum dots. *Adv Mater* 2010;22:734–8.

[25] Shen JH, Zhu YH, Chen C, Yang XL, Li CZ. Facile preparation and upconversion luminescence of graphene quantum dots. *Chem Commun* 2011;47:2580–2.

[26] Li Y, Hu Y, Zhao Y, Shi GQ, Deng L, Hou YB, et al. An electrochemical avenue to green–luminescent graphene quantum

dots as potential electron-acceptors for photovoltaics. *Adv Mater* 2011;23:776-80.

[27] Luo J, Cote LJ, Tung VC, Tan ATL, Goins PE, Wu J, et al. Graphene oxide nanocolloids. *J Am Chem Soc* 2010;132:17667-9.

[28] Lee J, Kim K, Park WI, Kim B-H, Park JH, Kim T-H, et al. Uniform graphene quantum dots patterned from self-assembled silica nanodots. *Nano Lett* 2012;12:6078-83.

[29] Kwon W, Kim Y-H, Lee C-L, Lee M, Choi HC, Lee T-W, et al. Electroluminescence from graphene quantum dots prepared by amidative cutting of tattered graphite. *Nano Lett* 2014;14:1306-11.

[30] Dong Y, Chen C, Zheng X, Gao L, Cui Z, Yang H, et al. One-step and high yield simultaneous preparation of single- and multi-layer graphene quantum dots from CX-72 carbon black. J Mater Chem 2010;22:8764-6.

[31] Ye R, Xiang C, Lin J, Peng Z, Huang K, Yan Z, et al. Coal as an abundant source of graphene quantum dots. *Nat Commun* 2013;4:2943.

[32] Liu R, Wu D, Feng X, Müllen K. Bottom-up fabrication of photoluminescent graphene quantum dots with uniform morphology. *J Am Chem Soc* 2011;133:15221-3.

[33] Wu JS, Pisula W, Müllen K. Graphenes as potential material for electronics. *Chem Rev* 2007;107:718-47.

[34] Yan X, Cui X, Li LS. Synthesis of large, stable colloidal graphene quantum dots with tunable size. *J Am Chem Soc*

2010;132:5944-5.

[35] Tang L, Ji R, Cao X, Lin J, Jiang H, Li X, et al. Deep ultraviolet photoluminescence of water-soluble self-passivated graphene quantum dots. *ACS Nano* 2012;6:5102-10.

[36] Dong Y, Shao J, Chen C, Li H, Wang R, Chi Y, et al. Blue luminescent graphene quantum dots and graphene oxide prepared by tuning the carbonization degree of citric acid. *Carbon* 2012;50:4738-43.

[37] Habiba K, Makarov VI, Avalos J, Guinel MJF, Weiner BR, Morell G. Luminescent graphene quantum dots fabricated by pulse laser synthesis. *Carbon* 2013;64:341-50.

[38] Lu J, Yeo PSE, Gan CK, Wu P, Loh KP. Transforming C_{60} molecules into graphene quantum dots. *Nat Nanotechnol* 2011;6:247-52.

[39] Geim AK, Novoselov KS. The rise of graphene. *Nat Mater* 2007;6:183-91.

[40] Radovoc LR, Bockrath B. On the chemical nature of graphene Edges: Origin of stability and potential for magnetism in carbon materials. *J Am Chem Soc* 2005;127:5917-27.

[41] Kim J, Suh JS. Size-controllable and low-cost fabrication of graphene quantum dots using thermal plasma jet. *ACS Nano* 2012;8:4190-6.

[42] Dolmans DE, Fukumura D, Jain RK. Photodynamic therapy for cancer. *Nat Rev Cancer* 2003;3:380-7.

[43] Castano AP, Mroz P, Hamblin MR. Photodynamic therapy

and anti-tumour immunity. *Nat Rev Cancer* 2006;6:535-45.

[44] Moore CM, Pendse D, Emberton M. Photodynamic therapy for prostate cancer—a review of current status and future promise. *Nat Clin Pract Urol* 2009;6:18-30.

[45] Lovell JF, Liu TWB, Chen J, Zheng G. Activatable photosensitizers for imaging and therapy. *Chem Rev* 2010;110:2839–57.

[46] Gao XH, Cui YY, Levenson RM, Chung LWK, Nie SM. *In vivo* cancer targeting and imaging with semiconductor quantum dots. *Nat Biotechnol* 2004;22:969–76.

[47] Michalet X, et al. Quantum dots for live cells, *in vivo* imaging, and diagnostics. *Science* 2005;307:538–44.

[48] Resch-Genger U, Grabolle M, Cavaliere-Jaricot S, Nitschke R, Nann T. Quantum dots versus organic dyes as fluorescent labels. *Nat Mathods* 2008;5:763–75.

[49] Ye L, et al. A pilot study in non-human primates shows no adverse response to intravenous injection of quantum dots. *Nat Nanotech* 2012;7:453–8.

[50] Bakalova R, Ohba H, Zhelev Z, Ishikawa M, Baba Y. Quantum dots as photosensitizers. *Nat Biotechnol* 2004;22:1360–1.

[51] Idris NM, et al. *In vivo* photodynamic therapy using upconversion nanoparticles as remote-controlled nanotransducers. *Nat Med* 2012;18:1580–5.

[52] Xiao L, Gu L, Howell SB, Sailor MJ. Porous silicon nanoparticle photosensitizers for singlet oxygen and their

phototoxicity against cancer cells. *ACS Nano* 2011;5:3651–9.

[53] Samia ACS, Chen XB, Burda C. Semiconductor quantum dots for photodynamic therapy. *J Am Chem Soc* 2003;125:15736–7.

[54] Ge J, et al. A graphene quantum dot photodynamic therapy agent with high singlet oxygen generation. *Nat Comm* 2014;5:4596–609.

[55] Lee MW, Kim J, Suh JS. Characteristics of graphene quantum dots determined by edge structures: three kinds of dots fabricated using thermal plasma jet. *RSC Adv* 2015;5:67669–75.

[56] Novoselov KS, Jiang Z, Zhang Y, Morozov SV, Stormer HL, Zeitler U, et al. Room–temperature quantum Hall effect in graphene. *Science* 2007;315:1379.

[57] Zhang Y, Tan Y–W, Stormer HL, Kim P. Experimental observation of the quantum Hall effect and Berry's phase in graphene, *Nature* 2005;438:201–4.

[58] Novoselov KS, Geim AK, Morozov SV, Jiang D, Katsnelson MI, Grigorieva IV, et al. Two–dimensional gas of massless Dirac fermions in graphene. *Nature* 2005;438:197–200.

[59] Katsnelson MI, Novoselov KS, Geim AK. Chiral tunnelling and the Klein paradox in graphene. *Nature Phys* 2006;2:620–5.

[60] Stankovich S, Dikin DA, Dommett GHB, Kohlhaas KM, Zimney EJ, Stach EA, et al. Graphene–based composite materials. *Nature* 2006;442:282–6.

[61] Liao L, Bai J, Qu Y, Huang Y, Duan X. Single–layer graphene on Al_2O_3/Si substrate: better contrast and higher performance of

graphene transistors. *Nanotech* 2010;21:015705.

[62] Watcharotone S, Dikin DA, Stankovich S, Piner R, Jung I, Dommett GHB, et al. Graphene–silica composite thin films as transparent conductors. *Nano Lett* 2007;7(7):1888–92.

[63] Wang X, Zhi L, Müllen K. Transparent, conductive graphene electrodes for dye–sensitized solar cells. *Nano Lett* 2008;8(1):323–7.

[64] Hao J, Liao Y, Zhong Y, Shu D, He C, Guo S, et al. Three–dimensional graphene layers prepared by a gas–foaming method for supercapacitor applications. *Carbon* 2015;94:879–87.

[65] Feng ZH, Yu C, Li J, He ZZ, Song XB, Wang JJ, et al. An ultra clean self–aligned process for high maximum oscillation frequency graphene transistors. *Carbon* 2014;75:249–54.

[66] Schedin F, Geim AK, Morozov SV, Hill EW, Blake P, Katsnelson MI, et al. Detection of individual gas molecules adsorbed on graphene. *Nature Mater* 2007;6:652–5.

[67] Li X, Wang X, Zhang L, Lee S, Dai H. Chemically derived, ultrasmooth graphene nanoribbon semiconductors. *Science* 2008;319:1229–32.

[68] Kosynkin DV, Higginbotham AL, Sinitskii A, Lomeda JR, Dimiev A, Price BK, et al. Longitudinal unzipping of carbon nanotubes to form graphene nanoribbons. *Nature* 2009;458:872–6.

[69] Gupta V, Chaudhary N, Srivastava R, Sharma GD, Bhardwaj R, Chand S. Luminescent graphene quantum dots for organic photovoltaic devices. *J Am Chem Soc* 2011;133(26):9960–3.

[70] Zhu S, Tang S, Zhang J, Yang B. Control the size and surface chemistry of graphene for the rising fluorescent materials. *Chem Commun* 2012;48:4527-39.

[71] Schniepp HC, Li J-L, McAllister MJ, Sai H, Herrera-Alonso M, Adamson DH, et al. Functionalized single graphene sheets derived from splitting graphite oxide. *J Phys Chem B* 2006;110(17):8535-9.

[72] Kim J, Heo SB, Gu GH, Suh JS. Fabrication of graphene flakes composed of multi-layer graphene sheets using a thermal plasma jet system. *Nanotech* 2010;21(9):095601.

[73] McDonough JK, Gogotsi Y. Carbon Onions: Synthesis and Electrochemical Applications. *Electrochem Soc Interface* 2013;22(3):61-6.

[74] Zeiger M, Jackel N, Mochalin VN, Presser V. Review: carbon onions for electrochemical energy storage. *Journal of Materials Chemistry A* 2016;4(9):3172-96.

[75] Pech D, Brunet M, Durou H, Huang P, Mochalin V, Gogotsi Y, Taberna PL, Simon P. Ultrahigh-power micrometre-sized supercapacitors based on onion-like carbon. *Nat Nanotechnol* 2010;5(9):651-4.

[76] Plonska-Brzezinska ME, Echegoyen L. Carbon nano-onions for supercapacitor electrodes: recent developments and applications. *Journal of Materials Chemistry A* 2013;1(44):13703-14.

[77] Butenko YV, Siller L, Hunt MRC. Carbon onions. InCarbon Nanomaterials, 406 2 ed.; Gogotsi Y; Presser V, Eds. CRC Press:

pp. 1–18, 2013.

[78] Anjos DM, McDonough JK, Perre E, Brown GM, Overbury SH, Gogotsi Y, Presser V, Pseudocapacitance and performance stability of quinone–coated carbon onions. *Nano Energy* 2013;2(5):702–12.

[79] Ugarte D. Curling and closure of graphitic networks under electron–beam irradiation. *Nature* 1992;359:707–9.

[80] Kuznetsov VL, Chuvilin AL, Butenko YV, Mal'kov IY, Titov VM. Raman and photoluminescence spectra of diamond particles with 1–5 nm diameter. *Chem Phys Lett* 1994;222:343–8.

[81] Mochalin VN, Shenderova O, Ho D, Gogotsi Y. The properties and applications of nanodiamonds. *Nat Nanotechnol* 2012;7:11–23.

[82] Sano N, Wang H, Chhowalla M, Alexandrou I, Amaratunga GAJ. Nanotechnology: Synthesis of carbon 'onions' in water. *Nature* 2001;414:506–7.

[83] Alexandrou I, Wang H, Sano N, Amaratunga GAJ. Structure of carbon onions and nanotubes formed by arc in liquids. *J Chem Phys* 2004;120:1055–8.

[84] Han F–D, Yao B, Bai Y–J. Preparation of carbon nano–onions and their application as anode materials for rechargeable lithium–ion batteries. J *Phys Chem C* 2011;115:8923–7.

[85] Ghosh M, Sonkar SK, Saxena M, Sarkar S. Carbon nano–onions for imaging the life cycle of Drosophila melanogaster. *Small* 2011;7:3170–7.

[86] Choucair M, Stride JA. The gram-scale synthesis of carbon onions. *Carbon* 2012;50:1109-15.

[87] Keller N, Maksimova NI, Roddatis VV, Schur M, Mestl G, Butenko YV, Kuznetsov VL, Schlögl R. The catalytic use of onion-like carbon materials for styrene synthesis by oxidative dehydrogenation of ethylbenzene. *Angew Chem Int Ed* 2002;41:1885-8.

[88] Su D, Maksimova NI, Mestl G, Kuznetsov VL, Keller V, Schlögl R, Keller N. Oxidative dehydrogenation of ethylbenzene to styrene over ultra-dispersed diamond and onion-like carbon. *Carbon* 2007;45:2145-51.

[89] Cabioćh T, Thune E, Rivière JP, Camelio S, Girard JC, Guérin P, Jaouen M, Henrard L, Lambin P. Structure and properties of carbon onion layers deposited onto various substrates. *J Appl Phys* 2002;91:1560-7.

[90] Hirata A, Igarashi M, Kaito T. Study on solid lubricant properties of carbon onions produced by heat treatment of diamond clusters or particles. *Tribol Int* 2004;31:899-905.

[91] Street KW, Marchetti M, Vander Wal RL, Tomasek AJ. Evaluation of the tribological behavior of nano-onions in Krytox. *Tribol Lett* 2004;16:143-9.

[92] Matsumoto N, Joly-Pottuz L, Kinoshita H, Ohmae N. Application of onion-like carbon to micro and nanotribology. *Diamond Relat Mater* 2007;16:1227-30.

[93] Joly-Pottuz L, Bucholz EW, Matsumoto N, Phillpot SR, Sinnott SB, Ohmae N, Martin JM. Friction Properties of carbon

nano-onions from experiment and computer simulations. *Tribol Lett* 2010;37:75-81.

[94] Koudoumas E, Kokkinaki O, Konstantaki M, Couris S, Korovin S, Detkov P, Kuznetsov V, Pimenov S, Pustovoi V. Onion-like carbon and diamond nanoparticles for optical limiting. *Chem Phys Lett* 2002;357:336-40.

[95] Sek S, Breczko J, Plonska-Brzezinska ME, Wilczewska AZ, Echegoyen L. STM-based molecular junction of carbon nano-onion. *ChemPhysChem* 2013;14: 96-100.

[96] Bartelmess J, Giordani S. Carbon nano-onions (multi-layer fullerenes): chemistry and applications. *Beilstein J Nanotechnol* 2014;5:1980-98.

[97] Shim J, Yun JM, Yun T, Kim P, Lee KE, Lee WJ, et al. Two-minute assembly of pristine large-area graphene based films. *Nano Lett* 2014;14(3):1388-93.

[98] Kim H-Y, Rho W-Y, Lee HY, Park YS, Suh JS. Aggregation effect of silver nanoparticles on the energy conversion efficiency of the surface plasmon-enhanced dye-sensitized solar cells. *Sol Energy* 2014;109:61-9.

[99] Costa DRD, Chaves A, Zarenia M, Pereira Jr JM, Farias GA, Peeters FM. Geometry and edge effects on the energy levels of graphene quantum rings: A comparison between tight-binding and simplified Dirac models. *Phys Rev B* 2014;89:075418.

[100] Grujić M, Zarenia M, Chaves A, Tadić M, Farias GA, Peeters FM. Electronic and optical properties of a circular graphene quantum dot in a magnetic field: Influence of the

boundary conditions. *Phys Rev B* 2011;84:205441

[101] Terasaka T, Toshiki M. A new expression for the vibrational overlap integrals between arbitrary one-dimensional harmonic oscillators. *Chem Phys Lett* 1981;80:306-310.

[102] Condon EU. Nuclear Motions Associated with Electron Transitions in Diatomic Molecules. *Phys Rev* 1928;32:858.

[103] Huang JY, Ding F, Yakobson BI, Lu P, Qi L, Li J. In situ observation of graphene sublimation and multi-layer edge reconstructions. *Proc Natl Acad Sci U.S.A.* 2009;106(25):10103-8.

[104] Kim I, Siddik M, Shin J, Biju KP, Jung S, Hwang H. Low temperature solution-processed graphene oxide/$Pr_{0.7}Ca_{0.3}MnO_3$ based resistive-memory device. *Appl Phys Lett* 2011;99:042101.

[105] Jang JW, Lee CE, Lyu SC, Lee TJ, Lee CJ. Structural study of nitrogen-doping effects in bamboo-shaped multiwalled carbon nanotubes. *Appl Phys Lett* 2004;84:2877-9.

[106] Ferrari AC, Meyer JC, Scardaci V, Casiraghi C, Lazzeri M, Mauri F, et al. Raman spectrum of graphene and graphene layers. *Phys Rev Lett* 2006;97:187401.

[107] Ferrari AC. Raman spectroscopy of graphene and graphite: disorder, electron-phonon coupling, doping and nonadiabatic effects. *Solid State Commun.* 2007;143(1-2):47-57.

[108] Casiraghi C, Pisana S, Novoselov KS, Geim AK, Ferrari AC. Raman fingerprint of charged impurities in graphene. *Appl Phys Lett* 2007;91:233108.

[109] Doumenc F, Boeck T, Guerrier B, Rossi M. Transient Rayleigh–Bénard–Marangoni convection due to evaporation: a linear non–normal stability analysis. *J Fluid Mech* 2010;648:521–39.

[110] Huang J, Kim F, Tao AR, Connor S, Yang P. Spontaneous formation of nanoparticle stripe patterns through dewetting. *Nat Mater* 2005;4:896–900.

[111] Fanton X, Cazabat AM. Spreading and instabilities induced by a solutal marangoni effect. *Langmuir* 1998;14(9):2554–61.

[112] Yang C, Bi H, Wan D, Huang F, Xie X, Jiang M. Direct PECVD growth of vertically erected graphene walls on dielectric substrates as excellent multifunctional electrodes. *J Mater Chem A* 2013;1:770–5.

[113] Wang H, Hu YH. Graphene as a counter electrode material for dye–sensitized solar cells. *Energy Environ Sci* 2012;5:8182–8.

[114] H. Choi, H. Kim, S. Hwang, Y. Han, M. Jeon, Graphene counter electrodes for dye–sensitized solar cells prepared by electrophoretic deposition, *J. Mater. Chem.* 21 (2011) 7548–7551.

[115] Zhang DW, Li XD, Li HB, Chen S, Sun Z, Yin XJ, et al. Graphene–based counter electrode for dye–sensitized solar cells. *Carbon* 2011;49(15):5382–8.

[116] Kaniyoor A, Ramaprabhu S. Thermally exfoliated graphene based counter electrode for low cost dye sensitized solar cells. *J Appl Phys* 2011;109:124308.

[117] Bajpai R, Roy S, Kumar P, Bajpai P, Kulshrestha N, Rafiee J, et al. Graphene supported platinum nanoparticle counter-electrode for enhanced performance of dye-sensitized solar cells. *ACS Appl Mater Interfaces* 2011;3(10):3884-9.

[118] Wu M, Lin X, Wang Y, Wang L, Guo W, Qi D, et al. Economical Pt-free catalysts for counter electrodes of dye-sensitized solar cells. *J Am Chem Soc* 2012;134(7):3419-28.

국문 초록

최근 고성능의 전자기기, 신재생 에너지 및 생명 의학을 발전시키기 위해 새로운 소재에 대하여 세계 각국의 연구자들이 관심을 갖고 있다. 많은 물질들이 신소재로서 각광을 받고 있지만 그 중에서 탄소나노소재는 독특한 구조와 특성에 의해 차세대 소재로서 많은 연구가 진행되고 있다. 탄소나노소재는 대표적으로 0차원 물질인 풀러렌 (fullerenes), 1차원 물질인 탄소나노튜브 (carbon nanotubes), 2차원 물질인 그래핀 (graphene)이 있으며 그 밖에도 그래핀 양자점 (graphene quantum dots), 양파구조탄소 (onion-type carbon), 비결정성탄소 (amorphous carbon), 나노다이아몬드 (nanodiamond), 탄소닷 (carbon dots) 등의 탄소나노소재가 있다. 탄소나노소재는 0차원 물질에서 3차원 물질까지 다양한 원자 구조를 가지고 있으며 그에 따라 각각의 다른 물질 특성을 가진다. 각각의 특성으로 탄소나노소재는 다양한 분야에 응용이 가능하다. 그러나 탄소나노소재의 상업화를 위해서는 대량 생산이 필수적이다. 본 연구에서는 열플라즈마 장치를 이용해서 탄소나노소재인 그래핀, 그래핀 양자점 및 양파구조탄소를 대량 제조하고, 제조된 물질의 특성 분석 및 응용에 대해서 서술하고자 한다.

그래핀은 현재 전 세계적으로 가장 관심 받고 있는 탄소나노소재 중 하나이며 연필심을 구성하고 있는 흑연 (graphite)과 탄소 이중결합을 뜻하는 “-ene”을 결합한 신조어이다. 그래핀은 탄소 원자들의 sp^2 결합으로 이루어진 2차원 물질이고 흑연에 한 층에 해당하지만 흑연과는 달리 새롭고 우수한 성질을

가진다. 2004년 영국 맨체스터 대학에서 그래핀을 스카치 테이프를 사용하여 분리하는데 성공하였으며 이후 2010년 그래핀 박리법으로 노벨상을 수상하였다. 그래핀의 특성으로는 실리콘의 100배 이상의 전자이동도와 강철보다 200배 이상의 강한 기계적 강도를 가지고 있다고 알려져 있다. 또한 그래핀은 신축성과 유연성이 우수하여 접거나 늘려도 전기전도성을 잃지 않는다는 장점을 가지고, 두께는 0.3 nm로 매우 얇은 물질로서 빛의 2.3% 만을 흡수한다. 또한 얇으면서도 매우 투명하다는 장점이 있다. 게다가 그래핀은 반금속성 특성을 띠며 가장 얇으면서도 은보다 열전도성이 우수하다고 알려져 있다. 그래핀 제조방법은 물리적 박리법 이후 물리/화학적 박리법, 화학기상증착법, 에피텍셜 성장법 등이 있다. 물리적 박리법은 그래핀을 처음으로 분리한 방법이기도 하며 테이프와 같은 물리적인 방법으로 탄소 소재에서 그래핀을 박리하는 방법이다. 그러나 이 방법은 대면적의 그래핀을 대량으로 생산하는 것이 어렵다는 단점이 있다. 물리/화학적 박리법은 용매를 이용하는 방법으로서 강산과 산화제를 이용하여 흑연에서 박리를 유도하고, 환원 과정을 거쳐 그래핀을 제조하는 방법이다. 그러나 물리/화학적 박리법은 그래핀을 대량 제조하기가 가장 유용하다고 알려져 있지만 강산을 이용한 산화로 인해 그래핀의 결함 및 산소 작용기의 제거가 어렵다는 단점이 있다. 이 단점으로 인해 그래핀의 우수한 특성들이 저하된다. 다음은 화학기상증착법이다. 이 방법을 이용한 그래핀 제조 방법은 고온에서 탄소에 쉽게 흡착되는 금속기판 위에 탄소원을 흘려준다. 고온 조건에서 탄소원이 금속 표면에서 결정화되어 그래핀이 제조된다. 이 방법은 대면적의 그래핀 제조가 가능하며 많은 회사들이 시제품을 생산하고 있다.

그러나 그래핀이 활용되기 위해 금속 에칭 및 transfer 등의 공정이 추가로 필요하며 그래핀 표면의 morphology를 조절하기가 어렵다는 단점이 있다. 에피택셜 성장법으로 그래핀을 제조하는 방법은 탄소의 결정구조를 갖는 재료를 고온에서 열처리를 하면 탄소가 결정 표면에 따라 그래핀이 생성된다. 그러나 이 에피택셜 성장법으로 제조된 그래핀은 물성이 좋지 않다는 단점이 있으며 공정이 복잡하다는 단점이 있다.

본 연구에서는 기존의 그래핀 제조에서의 단점을 보완하고 극복하고자 하였다. 열 플라즈마 장치로 그래핀을 제조하는 방법으로서 제조방법은 다음과 같다. 열 플라즈마 장치의 양극 끝에 긴 탄소봉을 부착하고 이 탄소봉과 수직하게 그리고 탄소봉 끝에서 어느 정도 간격을 두고 흑연 판을 위치시킨다. 이 후 양극과 음극 사이에 플라즈마 가스를 흘려주면서 고전압을 가하고 발생된 플라즈마 빔에 탄소원 물질을 주입하면 탄소원자 빔이 형성된다. 부착된 긴 탄소봉을 통과하는 동안 탄소원자 빔의 에너지가 감소하며 적당한 에너지를 가진 탄소원자 빔이 흑연 판에 연속적으로 충돌할 때 흑연 판의 표면 결정 구조의 영향을 받아 그래핀이 형성된다. 형성된 그래핀은 플라즈마 기체에 의하여 벗겨진다. 이로 인해 생성과 벗겨짐이 반복되면서 연속적으로 그래핀이 제조되는 원리이다. 이와 같이 열 플라즈마 장치를 이용하여 그래핀을 제조 할 경우 탄소원 물질을 연속적으로 공급할 수 있기 때문에 그래핀을 연속 및 대량 생산 할 수 있다. 열 플라즈마 장치로 그래핀 제조 시, 고온에서 합성이 이루어지기 때문에 고결정성을 갖는 순수한 그래핀을 제조할 수 있으며 결함을 최소화 할 수 있다. 제조된 그래핀은 박막형태로 필름을 제조하는데

성공하였으며 이 그래핀 박막은 염료감응 태양전지의 상대 전극으로 사용되었다. 이 그래핀 박막 전극은 기존의 백금 전극과 비교하여 경제적일 뿐 만 아니라 비슷한 광효율을 보여주었다.

그래핀은 우수한 전기전도도, 신축성, 유연성, 기계적 강도, 열전도도 등으로 많은 연구자들에게 각광받고 있다. 그러나 그래핀은 밴드갭을 가지지 않기 때문에 반도체에서의 응용에서 한계가 있다. 그래핀의 크기가 100 nm 이하 됨으로 밴드갭을 갖게 되고, 양자점과 같은 특성을 갖게 되는데 이를 그래핀 양자점이라고 한다. 그래핀 양자점은 나노미터 크기의 sp^2-sp^2 탄소 결합을 하며 크기에 따라 밴드갭을 조절할 수 있고 대면적의 그래핀과는 달리 가장자리에 영향을 받아 구조나 기능기에 의해 밴드갭을 조절할 수 있다고 알려져 있다. 일반적으로 그래핀 양자점은 광발광에 의해 푸른 계열의 빛을 발현하는데 크기가 커짐에 따라서 붉은 계열의 광발광하는 연구가 된 바 있다. 또한 가장자리 영향의 특성으로 그래핀 양자점은 두 가지 구조를 갖는다고 알려져 있다. 하나는 극성을 띄며 비공유 전자쌍을 갖고 지그재그 구조를 갖는 구조이며 다른 하나는 비극성을 띄며 삼중결합을 갖고 암체어 구조를 갖는 구조이다. 그래핀 양자점은 이 두 가지 구조 중 하나를 갖게 되는데 반응성, 광발광 특성에서 전혀 다른 성질을 갖는다고 알려져 있다. 일반적인 그래핀 양자점의 고유특성으로는 매우 투명하며, 강한 광발광을 나태내고 높은 표면적, 적은 독성, 그리고 다양한 용매에 분산이 우수하다고 알려져 있다. 이를 이용하여 에너지 및 바이오 분야 등에 응용이 연구 된 바가 있다. 그래핀 양자점의 제조하는 방법은 크게 두 가지로 나뉜다. 하나는 top-down method이며 다른 하나는 bottom-up method이다. Top-down method는 흑연,

산화흑연, 석탄 등 큰 사이즈의 탄소소재에서 대게 hummers method를 통해 수 나노미터의 그래핀 양자점을 제조하는 방법이며 bottom-up method는 aromatic ring을 가진 compound를 이용해서 그래핀 양자점을 제조하는 방법이다. 그러나 이 방법은 반응 중에서 탄소사이에 결함이 생길 수 있는 단점이 있다. 또한 제조 중 탄소와 탄소사이에 산소가 포함되어 그래핀 양자점의 고유 특성을 저하시킬 수 있다. 그래서 그래핀 양자점의 제조에서 품질을 개선하기 위해 많은 연구가 진행되고 있다. 본 연구실에서는 고품질의 그래핀 양자점을 제조하기 위해 열플라즈마 장치를 개발하고 그래핀 양자점 제조에 성공하였다. 열 플라즈마 장치를 그래핀 제조와는 다르게 과량의 탄소원 물질을 주입하여 탄소봉 내에서 탄소원자들 간의 충돌로 인해 그래핀 양자점을 제조한다. 이 제조법은 플라즈마 가스와 탄소원만으로 제조되기 때문에 고품질의 그래핀 양자점을 제조할 수 있다. 제조된 그래핀 양자점은 최초로 서로 다른 형태의 edge(지그재그형, 암체어형, 그리고 그들이 결합된 형태)를 갖는 그래핀 양자점을 추출함으로써 현재 이론적으로만 증명 및 분석된 edge effect를 화학적/전기적 특성에 따라 구체화 시켰다. 탄소원자들이 기체상 충돌로 평면 구조의 그래핀 양자점이 만들어 질 때 생기는 그래핀 양자점의 기본적인 모양은 육각형 모양과 사각형 모양이며, 가장자리 구조는 암체어 구조로부터 만들어지는 carbyne 구조와 지그재그 구조로부터 만들어지는 carbene 구조로 나누어진다. carbyne 구조는 삼중결합이 존재하며 비극성을 띠나 carbene 구조에는 비공유전자쌍이 존재하며 극성을 띤다. 육각형 모양의 그래핀 양자점의 가장자리는 모든 변이 carbyne 구조이거나 혹은 모든 변이 carbene 구조를

가진다. 그러나 사각형 모양의 그래핀 양자점은 서로 맞닿은 두 변은 한 변이 carbyne 구조를 가지면 다른 한 변은 carbene 구조를 가진다. 그래핀 양자점은 가장자리에 carbene 구조를 가지면 극성을 띠며 상대적으로 높은 밴드갭을 가지나 가장자리에 carbyne 구조를 가지면 비극성을 띠며 상대적으로 낮은 밴드갭을 가진다. 사각형 모양의 그래핀 양자점은 서로 마주보는 두 변은 carbyne 구조를 그리고 다른 두 변은 carbene 구조를 가져 carbyne 구조와 carbene 구조의 특성이 모두 나타난다. 따라서 그래핀 양자점이 서로 다른 극성을 가진 특성을 기반으로 서로 다른 극성의 용매를 사용하여 세 종류의 그래핀 양자점 추출 및 분석을 연구하였으며 그래핀 양자점의 edge effect를 실험적으로 증명하였다. 또한 제조된 지그재그 및 암체어 그래핀 양자점을 이용하여 생명의학 연구를 수행하였다.

양파구조탄소(onion-type carbon)는 과거에 나노다이아몬드와 함께 긴 시간 동안에 가장 유망한 탄소나노소재였다. 그러나 양파구조탄소는 다양한 장점에도 불구하고 제조 및 응용연구가 부족한 실정이다. 현재 그래핀과 탄소나노튜브 사용하여 많은 연구자들이 다양한 응용을 하고 있다. 특히 인류 최대의 관심 연구분야 중 하나인 암 치료에서 탄소나노소재의 광열 효과를 이용하여 치료에 대한 연구를 진행되고 있다. 그러나 연구과정에서의 독성 혹은 높은 비용과 같은 단점이 존재한다. 이러한 문제를 극복하고자 본 연구에서는 우수한 분산성, 낮은 독성, 그리고 높은 생산성의 양파구조탄소 물질을 제조하여 빛으로 암을 치료하는 응용 가능성을 확인하였다. 양파구조탄소 물질을 제조하는 방법은 다양한 방법이 있지만 그 중 일반적인 제조방법인

나노다이아몬드로의 어닐링으로부터 양파구조탄소 물질을 대량생산하는 것이다. 이 양파구조탄소 물질의 제조법은 산업적인 응용에 가능성을 열어 주었으며 순도는 거의 100%에 가까웠다. 제조된 물질은 거의 원형에 가까운 탄소였고 크기는 나노다이아몬드의 크기에 따라 달랐다. 또 다른 양파구조탄소 물질의 제조법은 물에서의 두 흑연 전극사이의 아크 방전을 통해서 제조하였다. 이 제조 방법은 나노다이아몬드를 이용하여 제조된 양파구조탄소와 거의 비슷한 구조를 보여주었다. 이외에도 세계적으로 양파구조탄소를 제조하는 방법은 지속적인 연구가 진행되고 있으며 이 물질은 합성과정에서 조금씩 다른 특성을 보여준다. 그러나 양파구조탄소의 제조에서 고비용 및 장시간의 제조 과정으로 인해 응용 연구에서 어려움이 있다. 본 연구에서는 열플라즈마 장치를 이용하여 양파구조탄소를 경제적이고 쉽게 제조하였으며 이를 이용하여 광열효과로 암을 치료하는 가능성을 찾았다. 양파구조탄소를 제조하는 방법은 그래핀 양자점 제조에서 함께 제조되는 부속물이며 그래핀 양자점을 용매로 씻어내 분리한다. 크기는 15 - 20 나노미터이며 구조에서 양파의 단면적과 같은 구조를 보여준다. 제조된 양파구조탄소는 다양한 유기 용매에 분산이 우수하고 자외선에서 근적외선영역까지의 빛을 모두 흡수한다. 이 특성을 이용하여 양파구조탄소 용액에 근적외선 빛을 조사하여 열이 발생하는 것을 확인하였다. 이는 생체외 실험에서 양파구조탄소 물질의 용액을 인체에 주입하고 근적외선 빛을 노출시키면 암 세포를 파괴시킬 수 있는 가능성을 확인하였다.

Keywords : 탄소나노소재, 그래핀, 열플라즈마 장치, 그래핀 양자점,

양파구조탄소, 광역학 치료, 광열 치료, 염료감응 태양전지.

Student Number : 2014-22408